

OPEN ACCESS

Performance of the reconstruction and identification of high-momentum muons in proton-proton collisions at $\sqrt{s} = 13$ TeV

To cite this article: A.M. Sirunyan *et al* 2020 *JINST* **15** P02027

View the [article online](#) for updates and enhancements.



IOP | ebooksTM

Bringing together innovative digital publishing with leading authors from the global scientific community.

Start exploring the collection—download the first chapter of every title for free.

Performance of the reconstruction and identification of high-momentum muons in proton-proton collisions at $\sqrt{s} = 13$ TeV



The CMS collaboration

E-mail: cms-publication-committee-chair@cern.ch

ABSTRACT: The CMS detector at the LHC has recorded events from proton-proton collisions, with muon momenta reaching up to 1.8 TeV in the collected dimuon samples. These high-momentum muons allow direct access to new regimes in physics beyond the standard model. Because the physics and reconstruction of these muons are different from those of their lower-momentum counterparts, this paper presents for the first time dedicated studies of efficiencies, momentum assignment, resolution, scale, and showering of very high momentum muons produced at the LHC. These studies are performed using the 2016 and 2017 data sets of proton-proton collisions at $\sqrt{s} = 13$ TeV with integrated luminosities of 36.3 and 42.1 fb⁻¹, respectively.

KEYWORDS: Large detector systems for particle and astroparticle physics; Muon spectrometers; Particle identification methods; Particle tracking detectors

ARXIV EPRINT: [1912.03516](https://arxiv.org/abs/1912.03516)

Contents

1	Introduction	1
2	The CMS detector	2
3	Data samples and simulation	3
4	High-p_T muon reconstruction overview	4
4.1	Reconstruction	5
4.2	Muon radiative energy losses: showering	7
4.3	Identification	10
5	Efficiency measurements	11
5.1	High- p_T muon identification efficiency	12
5.2	Reconstruction efficiency	15
5.3	Combined L1 and HLT efficiency	17
5.4	The L1 trigger efficiency	21
6	Momentum assignment performance	24
6.1	Momentum performance in simulation	24
6.2	Momentum resolution from cosmic ray muons and collision events	27
6.3	Momentum scale from collision events	30
7	Summary	31
	The CMS collaboration	37

1 Introduction

One of the main tasks of the CMS experiment is to search for new phenomena in proton-proton (pp) collisions delivered by the CERN LHC. Good identification and precise measurement of muons, electrons, photons, and jets over a large energy range and at high instantaneous luminosities are necessary for these searches to be effective. In particular, searches for heavy gauge bosons such as the Z' [1, 2] and W' [3] rely on precise reconstruction of muons up to very high momentum. With the data recorded from pp collisions in Run 2 at $\sqrt{s} = 13$ TeV, corresponding to integrated luminosities of 36.3 fb^{-1} in 2016 and 42.1 fb^{-1} in 2017, the CMS detector has recorded a sufficiently large sample of higher-energy muons to allow the first detailed studies of such muons at the LHC, presented here. For some analyses that require an independent data set with all CMS subdetectors activated, the luminosities recorded are slightly lower with 35.9 fb^{-1} in 2016 and 41.5 fb^{-1} in 2017.

Previously published studies of the CMS muon detectors [4] and muon reconstruction [5] were based on data from pp collisions recorded during Run 1 in 2010 at $\sqrt{s} = 7$ TeV, as well as on data recorded in 2015 and 2016 at 13 TeV [6]. An extensive description of the performance of the muon detector and the muon reconstruction software is given in refs. [4, 5], while ref. [6] focuses on significant improvements made to the muon system during the long shutdown period in 2013–2014 between LHC Runs 1 and 2. These changes resulted in reconstruction software and the high-level trigger (HLT) that were shown to have similar or better performance than in 2010, despite the higher instantaneous luminosity.

In this paper, we present performance measurements of the muon triggering, reconstruction, identification, and momentum assignment, for muons with high transverse momentum $p_T > 200$ GeV. Above this threshold, the effects of radiative energy losses in the steel flux-return yoke of the solenoid due to pair production, bremsstrahlung, and photonuclear interactions, as well as detector alignment, become significant enough to motivate dedicated studies.

Various sources of high-momentum muons are used to ensure significant and meaningful results. We include muons from the decays of high-mass off-shell standard model (SM) vector bosons, denoted as high-mass Drell-Yan events (DY), and muons from the decay of on-shell W or Z bosons recoiling against jets, denoted as Z (W)+jets events. In addition, we study high-momentum muons originating from cosmic rays, recorded during both the pp collisions and dedicated periods with no beam.

2 The CMS detector

The central feature of the CMS apparatus is a superconducting solenoid of 6 m internal diameter, providing a magnetic field of 3.8 T. Within the solenoid volume are a silicon pixel and strip tracker, a lead tungstate crystal electromagnetic calorimeter (ECAL), and a brass and scintillator hadron calorimeter (HCAL), each composed of a barrel and two endcap sections. Forward calorimeters extend the coverage in pseudorapidity η provided by the barrel and endcap detectors. Muons are detected in gas-ionization chambers embedded in the steel flux-return yoke outside the solenoid.

Events of interest are selected using a two-tiered trigger system [7]. The first level (L1), composed of custom hardware processors, uses information from the calorimeters and muon detectors to select events at a rate of around 100 kHz within a fixed time interval of less than 4 μ s. The second, high-level trigger (HLT) consists of a farm of processors running a version of the full event reconstruction software optimized for fast processing, and reduces the event rate to around 1 kHz before data storage.

Muons are measured in the range $|\eta| < 2.4$ with detection planes made using three technologies: drift tubes (DTs), cathode strip chambers (CSCs), and resistive plate chambers (RPCs). The single-muon trigger efficiency with respect to reconstructed muons exceeds 90% over the full η range with respect to reconstructed muons, and the efficiency to reconstruct and identify muons that pass the trigger requirements is greater than 96%. Matching muons to tracks measured in the silicon tracker results in a relative p_T resolution of 1% in the barrel and 3% in the endcaps, for muons with p_T up to 100 GeV. The p_T resolution in the barrel is better than 7% for muons with p_T up to 1 TeV [6].

At the end of the 2016 LHC running period, an additional pixel layer was added to the tracker; the HLT sequences were modified to sustain a higher rate due to the increase of the number of

pp interactions in the same or adjacent bunch crossings, referred to as pileup; and the detector was opened and the alignment conditions were consequently changed. These modifications could impact several studies performed in this paper; whenever it appears to be the case, it is explicitly mentioned.

A more detailed description of the CMS detector, together with a definition of the coordinate system used and the relevant kinematic variables, can be found in ref. [8].

3 Data samples and simulation

The studies described in this paper are mostly based on data recorded using single-muon triggers. In addition, for the trigger studies, we use data samples recorded with single-electron triggers and missing transverse momentum (p_T^{miss}) triggers, referred to as independent data sets, since they provide unbiased samples of muons suitable for studies of muon triggers. (We follow common usage in defining p_T^{miss} as the magnitude of the projection onto the plane perpendicular to the beam axis of the vector sum of the momenta of all reconstructed objects in an event.) To maximize the sample size at high momentum, the muon data sets from 2016 and 2017 are merged when the performance under study is independent of the detector and software changes from one year to another; otherwise, the results are presented for the two years separately. The results in this paper are obtained from selected data samples consisting of events with a pair of reconstructed muons, or with a single reconstructed muon for the trigger study using independent data sets; throughout, muon $p_T > 53$ GeV is required, in order to be above trigger turn-on effects at the trigger threshold of 50 GeV. Further event criteria are applied, depending on the study, and are described in detail below. Cosmic ray muon data, recorded in the absence of LHC beams or in gaps between pp collisions, are used to provide complementary studies on the muon momentum resolution and charge assignment.

The selected data events are compared with simulations from several event generators that use the Monte Carlo (MC) method. The DY $Z/\gamma^* \rightarrow \mu^+ \mu^-$ signal samples are generated with POWHEG v2 [9–11] at next-to-leading order (NLO) in both QCD and electroweak corrections, and cover a mass range from 50 GeV up to 5 TeV. For the studies that use exclusively the Z peak ($60 < m_{\mu\mu} < 120$ GeV) and explore the high-momentum muons produced from boosted bosons, we use samples enriched in Z+jets generated with MADGRAPH5_AMC@NLO v2.2.2 [12]. Finally, the $W^* \rightarrow \mu\nu$ signal samples, used to validate the single-muon trigger efficiency, are generated at leading-order (LO) with PYTHIA 8.212 (8.230) [13] for 2016 (2017) studies.

The dominant backgrounds over the full dimuon mass range are, in order of importance, $t\bar{t}$, tW , and WW ; they are simulated at NLO with POWHEG. The $t\bar{t}$ cross section is calculated at next-to-NLO (NNLO) with Top++ v2.0 [14]. Other electroweak backgrounds, such as WZ and ZZ , are generated with PYTHIA.

For all simulated samples mentioned above, the fragmentation and parton showering is modeled with PYTHIA 8.212 with the CUETP8M1 [15] underlying event tune for the 2016 studies or with PYTHIA 8.230 with CP5 [16] tune for 2017 studies. The NNPDF3.0 [17] and NNPDF3.1 [18] parton distribution function sets are used for the 2016 and 2017 samples, respectively. The simulation of the CMS detector response is based on GEANT4 [19]; the events are then reconstructed with the same algorithms as used for data. Pileup is also simulated, except for studies where it is explicitly stated that this is not the case.

4 High- p_T muon reconstruction overview

Most of the muons produced in CMS originate in processes such as semileptonic decays of top quarks or heavy-flavor hadrons, or in leptonic decays of on-shell vector bosons (W, Z). Such muons typically have $p_T < 200$ GeV, and are referred to as low- p_T muons. On the other hand, high- p_T muons are produced in rare processes such as off-shell production of high-mass or on-shell production of high- p_T W^{*} and Z^{*}/ γ bosons, and could be produced from the decay of beyond the standard model (BSM) particles with TeV-scale mass (e.g., Z' or W' bosons).

Experimentally, the main differences between high- and low- p_T muons can be understood as follows. As the muon momentum increases, the p_T resolution of the reconstructed track degrades. In the part of the orbit in near-uniform magnetic field B , the measurement of p_T depends on B , and the radius of curvature, R , of the track [20]:

$$p_T[\text{GeV}] = |0.3B[\text{T}]R[\text{m}]|. \quad (4.1)$$

The magnetic field is monitored with high precision and is roughly uniform at 3.8 T in the tracker volume inside the solenoid. The radius of curvature is related to the arc length L and sagitta s of the track via

$$R[\text{m}] \approx L[\text{m}]^2/8s[\text{m}], \quad (4.2)$$

where the approximation is valid for $L/R \ll 1$. Assigning arithmetic signs consistently to R , s , and the charge q (in units of proton charge) yields

$$s[\text{m}] \approx (0.3B[\text{T}]L[\text{m}]^2/8)(q/p_T[\text{GeV}]) = (0.3BL^2/8)\kappa, \quad (4.3)$$

where $\kappa = q/p_T$ is referred to as the (signed) curvature of the muon track. Because s is linearly related to the measurement of hit positions in the detector (which have approximately symmetric uncertainties), the uncertainty in κ (rather than in p_T) from the cumulative effect of hit uncertainties is (approximately) Gaussian. Hence κ is the more natural variable for use in muon momentum resolution and scale studies, as discussed in section 6. As the p_T increases and the sagitta in the tracker decreases, the muon momentum measurement can be improved by using the large BL^2 between the tracker and the muon system (and within the muon system), if the p_T is large enough that multiple Coulomb scattering in the calorimeters and in the steel flux-return yoke of the solenoid does not spoil the measurement. Thus high- p_T muon track reconstruction and muon momentum measurement rely on matching tracks reconstructed in the inner tracker and the muon system, separated by more than 3 meters and forming a global track, as explained in section 4.1. However, because of the smallness of the sagitta (or more precisely, the generalizations of sagitta in nonuniform B) in the TeV regime, the muon p_T resolution is sensitive to alignment of the hits used to reconstruct the muon track. The impact of the detector alignment on the momenta resolution is discussed in section 6.

If a muon traveling through the steel of the magnet flux-return yoke has sufficiently large momentum, radiative energy losses (bremsstrahlung with inner and outer e^+e^- pair production, photonuclear interactions) are no longer negligible compared to ionization energy losses. The muon critical energy for iron, E_c^{iron} , at which the ionization energy losses are equal to the sum of all radiative losses, is around 300 GeV [20]. As a consequence, the main source of energy loss

for muons above E_c^{iron} propagating through the steel between the muon subdetectors is radiative energy losses. This radiation creates cascades of particles (electromagnetic showers) and can lead to extra hits being reconstructed in the muon detectors. These showers can have a strong impact on the muon performance (i.e., triggering, reconstruction, or p_T measurement). The muon showering primarily depends on the total muon momentum, as opposed to the transverse component that is commonly used in physics analyses. Depending on the longitudinal component of momentum, muons with $p_T > 200$ GeV can have energies above E_c^{iron} . The potential presence of showers around the muon track is what motivates the choice of $p_T > 200$ GeV to define a high- p_T muon in the paper. Dedicated algorithms for momentum assignment have been developed and are discussed in section 4.1. In addition, in order to understand the behavior of high- p_T muons and the impact of showering along the CMS detection sequence, we parameterize the showering and then confront simulation with data on the various muon performance aspects. This shower tagging is discussed in section 4.2, whereas the results of the muon performance as a function of muon showering are shown in sections 5 and 6.

Some BSM searches, involving high- p_T muons, probe processes with small cross sections for which negligible backgrounds from SM processes are expected. High efficiency for measuring TeV muons is particularly important for obtaining a high sensitivity in such searches. For example, the current upper limit [21] on the product of production cross section and branching fraction for a Z' boson with a mass of 2 TeV, $\sigma(Z')\mathcal{B}(Z' \rightarrow \mu\mu)$, is $\mathcal{B}(10^{-7})$ smaller than that of the SM Z boson, $\sigma(Z)\mathcal{B}(Z \rightarrow \mu\mu)$. In such analyses, the signal efficiencies are derived with simulated samples. While the simulations can be validated in some kinematic regions using Z boson events in data, the lack of signal at higher masses forces the analysis strategy to extrapolate into the highest p_T regions. Therefore, it is important to have uniform reconstruction, identification, and triggering efficiencies as a function of the muon p and p_T , and to ensure that any sensitivity to muon showering is understood. Dedicated high- p_T muon identification criteria have been developed and further improved during LHC Run 2 in order to provide robustness with increasing muon p_T ; they are detailed in section 4.3. The level of agreement between the performance in data and simulation is quantified in terms of data-to-simulation efficiency ratios called scale factors (SF).

4.1 Reconstruction

In the standard CMS reconstruction procedure for pp collisions, muon tracks are first reconstructed independently in the inner tracker and in the muon systems [22]. In the latter, tracks called “standalone muons” are reconstructed by using information from DT, CSC, and RPC detectors along a muon trajectory using the Kalman filter technique [23]. In both the barrel and endcap regions, the muon detectors reside in four “stations”, which are typically separated by 23 to 63 cm of steel. The steel thickness prevents an electromagnetic shower from propagating across more than one station. Within each station, there are multiple planes of detectors, from which “hits” are recorded. The hits within a station are combined into local “segments”, which are in turn combined into standalone muons.

Matching standalone-muon tracks with tracks reconstructed in the inner tracker yields combined tracks referred to as “global muons”. If the momentum, direction, and position in the transverse plane of the inner and standalone tracks are compatible, then the global track is fit by combining hits from the tracker track and standalone-muon track in a common fit.

Global muons are complemented by objects referred to as “tracker muons” that are built by propagating the inner tracker tracks to the muon system with loose geometrical matching to DT or CSC segments. If at least one muon segment matches the extrapolated track, the track is qualified as a tracker muon. Tracker muons have higher efficiency than global muons in regions of the CMS detector with less instrumentation and for muons with low- p_T .

The momentum of a muon reconstructed as a global muon can be extracted from the combined tracker-plus-standalone trajectory. For high- p_T muons, however, extra particles produced in electromagnetic showers can contaminate the muon detectors, yielding extra reconstructed hits and segments. These extra segments can be picked up by the trajectory building algorithm instead of the correct muon track segment, or even make the reconstruction of the muon track in a chamber impossible. The high- p_T case thus requires careful treatment of the information from the muon system. A set of specially developed TeV-muon track refits has been developed to address this issue: the “tracker-plus-first-muon-station” (TPFMS) fit, the “Picky” fit, and the “dynamic truncation” (DYT) fit. The momentum assignment is finally performed by the “TuneP” algorithm, which chooses the best muon reconstruction among the tracker-only track, TPFMS, DYT, and Picky fits.

The TPFMS fit is historically the first alternative to the global muon fit (which is based on all the trajectory measurements). It only uses hits from the tracker and the innermost muon station containing hits, thus taking advantage of a large BL^2 , while neglecting the stations that are farther along the muon’s trajectory, thus reducing potential contamination from showers. Even with this omission, by making a judicious track-by-track choice between the tracker-only fit and the TPFMS fit, the resolution at high p_T can be improved with respect to both the tracker-only fit and the global fit [6].

Other strategies for improvement have also been developed. If a shower in one muon station corrupts the position measurement in that specific station, thus the thickness of the steel layer will absorb the shower and prevent it from leaking into the next station. Then, in principle, if it is possible to identify a station where a shower occurs, then it can be discarded from the muon global fit instead of rejecting most stations, as is done with TPFMS. The Picky algorithm was developed with this approach in mind. It identifies stations containing showers based on the hit multiplicity, and for each of them, it imposes extra requirements on hit compatibility with the muon trajectory. If hits in a station with showering fail these requirements, that station is removed from the trajectory fit.

The DYT fit approach is based on the observation that in some cases, when a muon loses a large fraction of its energy, its orbit can change and the segments (or hits) in subsequent stations may no longer be consistent with the initial trajectory. In other cases, where the energy loss is less severe, only hits in one station appear incompatible, while the rest of the trajectory is negligibly changed and can be used in the fit. The DYT algorithm starts from the tracker track and proceeds outwards, iteratively adding to the fit muon hits compatible with the extrapolated track trajectory. When incompatible hits are found it ignores them or stops the fit entirely, depending on the degree of incompatibility.

Thus, the algorithm for choosing between the tracker-only fit and TPFMS has evolved into a more general algorithm, known as the TuneP algorithm, for choosing among the various refits on a track-by-track basis. It uses the track fit χ^2/dof tail probability and the relative p_T measurement uncertainty σ_{p_T}/p_T , where σ_{p_T} is the uncertainty in p_T , as determined by the Kalman filter. The algorithm starts its search for the best track fit choice by initially considering the Picky hypothesis

and comparing its σ_{p_T}/p_T with the value estimated for the corresponding track but refitted by the DYT algorithm. The refit with the smallest uncertainty in p_T is then compared to the tracker-only fit, and the track with the lower χ^2/dof tail probability value is kept, to be finally compared with the TPFMS refitter algorithm. The final best track is chosen after the last comparison according to the χ^2/dof tail probability. In the rare cases where there is no convergence in the Picky algorithm refit, or in the other refits tried consecutively, the global fit is kept.

In cases where the final candidate track has a p_T lower than 200 GeV, the tracker-only fit is used. Figure 1 presents the fractions for each choice of TuneP among DYT, Picky, and any of the other fits (TPFMS, global, or tracker-only), as a function of the muon p_T , separately for the barrel and endcap regions. The selected muons come from dimuon events and are required to pass the high- p_T identification described in section 5.1, and to have $p_T > 200$ GeV. To simulate the data events, we add to DY simulation all the other electroweak processes that arise in data and that mimic DY events (diboson, $t\bar{t}$, single top quark, etc.). We do not add the background from SM events comprised uniquely of jets produced through the strong interaction, because this background is negligible above 200 GeV. The simulation reproduces well what is observed in data: similar fractions in the choice among the refits across the full p_T spectrum, with a preference for Picky in the barrel ($\approx 60\%$) while similar fractions for DYT and Picky are found in the endcaps ($\approx 50\%$). When DYT was first developed, its performance was studied integrated over muon η and in consequence found to be driven by the endcap region where most of the showering takes place. The high level of agreement between data and simulation is an indication that the impact of showering on momentum assignment is well reproduced by simulation.

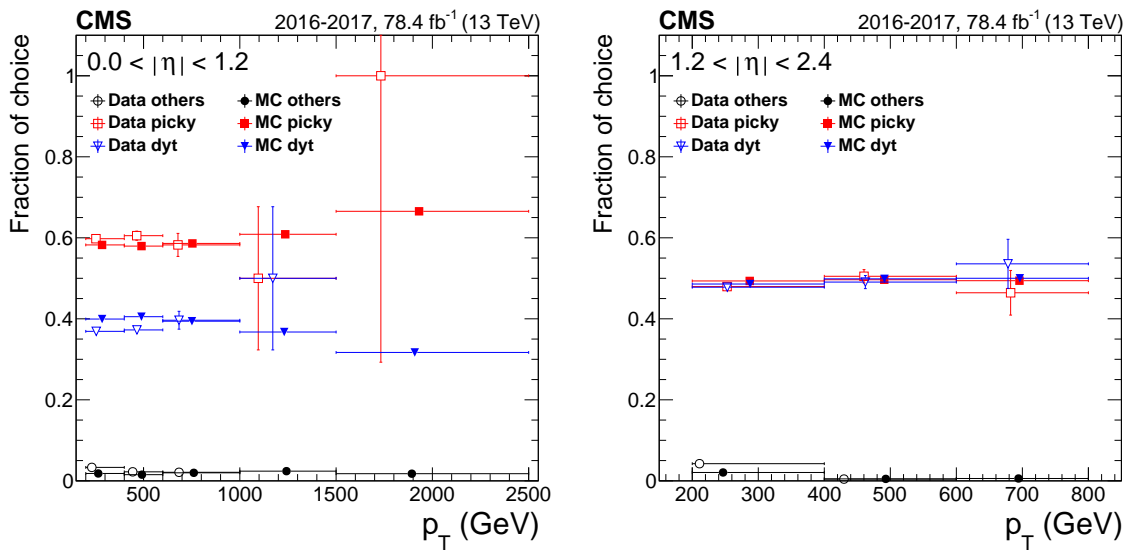


Figure 1. Fraction of choices of different refit algorithms chosen by TuneP, comparing 2016+2017 data and DY simulation for five p_T ranges and for two η categories: (left) barrel with $|\eta| < 1.2$ and (right) endcap with $1.2 < |\eta| < 2.4$. The central value in each bin is obtained from the average of the distribution within the bin.

4.2 Muon radiative energy losses: showering

In order to understand the effect of showers on the various aspects of muon reconstruction and measurements (including triggering) we have developed empirical definitions to identify (“tag”)

and characterize showers in the muon systems. Both data and simulation samples are used to converge on this definition of a “shower” and are compared to study the adequacy of the shower modeling in simulation.

The “extended tag-and-probe” technique (section 5) is used to study showers in simulated high-mass DY samples and in dimuon events from the single-muon primary data sets (section 3). Definitions for tags, probes, and dimuon pairs are the same as those used to measure muon reconstruction efficiency, and are described in detail in section 5.2. In addition, single-muon (or antiparallel double-muon) samples uniform in η and p in the range between 5 and 2500 GeV are generated without simulating pileup. In this case, the muon candidates used in the analysis are required to satisfy only the selection criteria used for probes, except that the muons are not required to come from the primary vertex, since it is problematic to accurately reconstruct a vertex with only two tracks that are nearly antiparallel.

The multiplicity of segments reconstructed within a single DT or CSC station can be used as a proxy to identify showers. The tracker track of the selected probes is extrapolated to the different station layers of the muon detectors. Segments belonging to the chambers traversed by the propagated track are counted if they lie within $|\Delta x| < 25$ cm from the extrapolated track position, with Δx computed in local chamber coordinates and representing the bending direction of the track. If the extrapolated track crosses a given station layer close to the border between chambers, or if different chambers overlap, segments satisfying the requirement on Δx in all potentially crossed chambers are counted. Finally, the number of track-segment matches, provided by the tracker muon identification for all the chambers involved in the computation, is also counted and subtracted from the total sum. The result of this logic is the number of *extra segments* (i.e., the number of segments in addition to those belonging to a muon track), computed independently for each station crossed by a muon. It is referred to as N_{seg} .

The DT and CSC local reconstruction can generate “ghosts”, i.e., reconstructed tracks with no corresponding genuine track, in cases of multiple track segments traversing a single chamber. For example, in the case of DTs, the segment fitting is first performed independently in the ϕ and θ views of a chamber and pairs of such “2D segments” are then combined only at a later step of the segment reconstruction to provide a three-dimensional object. Combinations are built out of all possible permutations of ϕ - θ 2D segments, leaving to the standalone track reconstruction the burden of the disambiguation. A similar phenomenon happens for CSCs, though with different logic due to a different approach to the segment building.

The value of N_{seg} above which a station is considered to have a shower was chosen after considering several possibilities. The probability to have at least one station with a shower increases with the muon momentum, while for very low momentum it should be close to zero. The slope of dependence is larger for a looser requirement on N_{seg} . However, when requiring $N_{\text{seg}} \geq 1$, the shower probability for very low momentum is still ≈ 20 – 30% , which suggests a large contribution from ghosts. This falls to ≈ 5 – 10% for $N_{\text{seg}} \geq 2$; consequently, the requirement $N_{\text{seg}} \geq 2$ is chosen as the working point for shower tagging, because this is the most sensitive definition having acceptably small mistagging of showers at low momentum.

The probabilities of finding a shower in each of the four muon stations are computed separately and are compatible, except in the first muon station in the endcap, where the shower probability is higher than in the remaining endcap stations by $\approx 20\%$. We attribute this to hadronic punch-through

hadrons from other collisions in the bunch crossing, wrongly tagged as muon-induced showers; this effect is not present in the single-muon simulated sample, which does not include pileup. For the purpose of the studies in this paper, we use a simple picture with one number characterizing the probability of tagging a shower in any station. Figure 2 shows the resulting probability $P_{\text{shower}}(p)$ to tag a shower in at least one of the four muon stations as a function of the muon momentum.

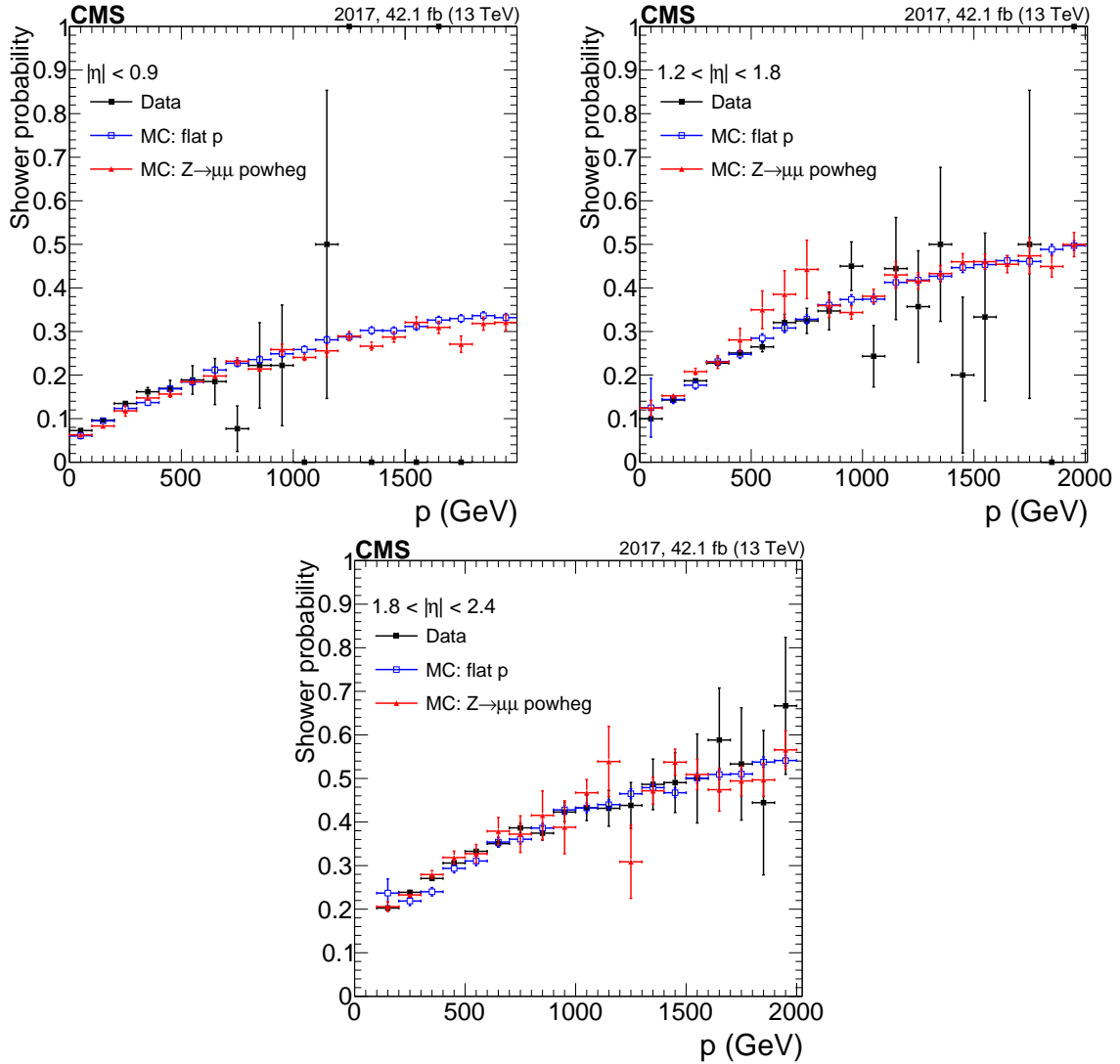


Figure 2. The probability $P_{\text{shower}}(p)$ to tag at least one shower in any of the four stations, as a function of the incoming muon momentum, for (upper left) DTs; (upper right) CSCs with muon $|\eta| < 1.8$; and (lower) CSCs with muon $|\eta| > 1.8$. Results are evaluated for the shower tagging definition requiring $N_{\text{seg}} \geq 2$. Different colors refer to: data (black), DY simulation (red), and single muons simulated with a uniform p distribution (blue).

Results from data are compared with those from the simulated high-mass DY and single-muon samples, in the barrel and endcap regions separately. The endcaps are further split above and below $|\eta| = 1.8$ to isolate the forward endcap region that has the highest shower probability. Below 1000 GeV there is good agreement between data and simulation, thus validating the modeling of showers in simulation.

4.3 Identification

High-momentum muons are produced in rare processes with low cross sections and backgrounds. Often in searches the muon identification performance is measured using simulation in TeV signal regions that is validated only with extrapolations from measurements at lower momenta. In order to make this procedure more robust, the muon identification efficiency is designed to be uniformly high as a function of muon p and p_T . For this purpose a dedicated high- p_T muon identification was designed during Run 1 [24] (“Run 1 high- p_T ID”), targeting topologies involving high- p_T muons; it was further improved during Run 2 (“Run 2 high- p_T ID”).

In the Run 1 high- p_T ID, muons are required to be global muons with at least two segments reconstructed in two muon stations that match the inner track. This selection suppresses punch-through and accidental track-to-segment matches. The main source of inefficiency is due to the gaps between the muon chambers and is more prominent in the barrel region, where CMS has two pathways (“chimneys”) for services located around $|\eta| = 0.3$. In contrast, chambers in the endcaps overlap with each other, which provides continuous coverage. The main update of this selection for Run 2 is to consider global muons that have only one segment matching the inner track, but only when the extrapolation from the tracker muon to the muon system predicts that they pass through the muon system gaps. In that case, only zero or one segment is expected to match the inner track. This change in the Run 2 high- p_T ID raises the signal efficiency by 1 to 2% at high p_T and improves agreement between the data and simulation. The efficiency gain affects high- p_T muons slightly more than lower- p_T muons because of a kinematic correlation: high- p_T muons are mostly produced from high-mass states that have low absolute rapidity and hence their muon decay products are more likely to be in the barrel region.

To guarantee that the muon system information is also used in the final momentum assignment, the Run 1 high- p_T ID requires that at least one valid muon system hit be retained in the global muon fit, which removes the outlier hits. The global muon valid hit collection is inherited from the parent standalone muon and the hits are qualified as valid when their addition to the global muon fit does not degrade the χ^2 . However, in the presence of showers, the hit multiplicity increases and the χ^2 of the standalone fit gets worse when trying to include them in the trajectory fit. The TuneP algorithm that has been developed to optimize the muon refit (section 4.1) can result in a hit collection used for the final momentum assignment that differs from the global hits collection; furthermore, if $p_T < 200$ GeV, the TuneP algorithm chooses the fit using only tracker hits. Hence, the second change from the Run 1 high- p_T ID to the Run 2 high- p_T ID consists in requiring that either the global muon fit or the fit chosen by TuneP use at least one valid muon system hit. This change raises the signal efficiency by 1% for muons with $p_T > 500$ GeV, mostly affecting the endcap region where showering (which scales with p , not p_T) is more abundant.

Figure 3 displays the Run 1 high- p_T ID efficiency as a function of muon η and p_T , with comparison to the Run 2 high- p_T ID efficiency. They are obtained from DY simulations and from dimuon events in data when combining the full 2016 and 2017 data sets. The method to compute these efficiencies as well as more details and results concerning the Run 2 high- p_T ID efficiency are discussed in section 5.1.

The other selection criteria of the Run 2 high- p_T ID are the same as for the Run 1 high- p_T ID, with notably tight requirements on the track part of the global muon. A minimal number of pixel

hits and tracker layers is required in order to ensure that the muon originates from the center of the primary interaction, to suppress cosmic ray muons and muons produced from meson decays in flight, and to ensure good momentum measurement resolution. Finally, a muon is required to have a reliable p_T assignment to perform the analysis; thus only global muons with a TuneP relative p_T measurement uncertainty, σ_{p_T}/p_T , smaller than 30% are considered.

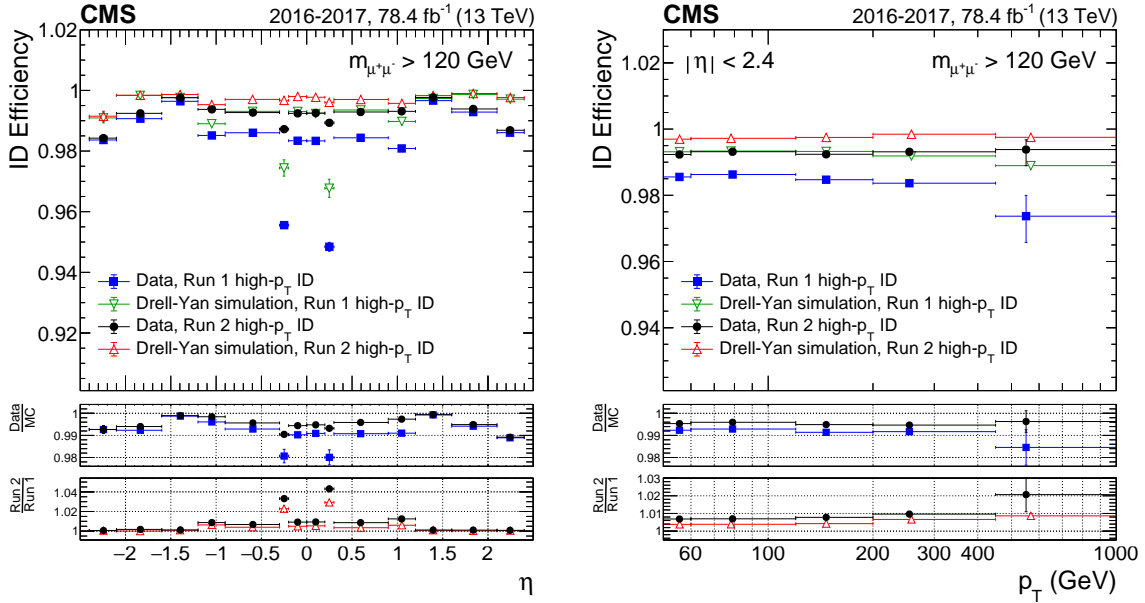


Figure 3. Comparison between the efficiency of Run 2 and Run 1 high- p_T ID, as a function of (left) η and (right) p_T . The efficiencies are obtained from dimuon events with a mass greater than 120 GeV to further select the high-mass DY process. The top panel shows the data to simulation efficiency ratio obtained for the Run 1 (blue squares) and for the Run 2 high- p_T ID (black circles). The bottom panel shows the Run 2 to Run 1 high- p_T ID efficiency ratio obtained from the data (black circles) and from simulation (red triangles). The central value in each bin is obtained from the average of the distribution within the bin.

5 Efficiency measurements

The tag-and-probe method [5] is a standard technique for measuring efficiencies for prompt muons coming from Z boson decays. The method provides an unbiased estimation of the total muon efficiency ϵ_μ at the various stages of muon trigger, offline muon tracking reconstruction, and muon identification. Each component of ϵ_μ is determined individually and factorized according to:

$$\epsilon_\mu = \epsilon_{\text{track}}\epsilon_{\text{ID}}\epsilon_{\text{reco}}\epsilon_{\text{trig}}. \quad (5.1)$$

The efficiency ϵ_{track} of the tracker track reconstruction appears independent of the muon momentum and does not require dedicated study at high momentum [25]. All other components of ϵ_μ rely on the performance of the muon system and can potentially be affected by muon showering as well as by the biases in the muon system alignment. Such features would lead to a dependence of efficiency on muon p_T and η . The individual components ϵ_{ID} , ϵ_{reco} , and ϵ_{trig} are scrutinized and

computed as functions of these kinematic variables in sections 5.1–5.3, respectively. In addition, in order to understand the impact of muon showering on the efficiency and to establish if the simulation models data accurately, the various efficiency components are studied as a function of showering, using the shower tagging method described in section 4.2. A slight difference with respect to the usual tag-and-probe method concerns ϵ_{reco} , where the probe is a tracker muon instead of a track. Starting from a track allows probing of the entire muon system reconstruction, whereas for the tracker muon requirement, there is already the assumption that at least two segments are reconstructed in the muon chambers and that they are aligned with the track. We have checked that this difference has a negligible impact and no p dependence. To gain further insight into the combined L1 and HLT efficiency of section 5.3, separate L1 efficiency studies are presented in section 5.4.

In order to compute ϵ_{μ} up to p_{T} of 1 TeV, the standard tag-and-probe method has been augmented. In this “extended tag-and-probe” method, we aim to collect as many prompt high- p_{T} muons from the DY process as possible with maximal suppression of backgrounds. Therefore, we do not restrict the invariant mass of the tag and probe muons to the Z boson mass window. For background rejection, we impose very tight isolation requirements on both tag and probe muons. The isolation requirements rely exclusively on the energy measured in the tracker, in a cone centered on the muon track and with a radius $\Delta R = \sqrt{(\Delta\eta)^2 + (\Delta\phi)^2}$ smaller than 0.3. No inputs from the calorimeters are considered in the computation of isolation, to avoid including radiation emitted by the muon that could bias the shower studies. Only muons with total energy in the cone smaller than 30 GeV and not more than 5% of their p_{T} are kept. In addition to the isolation selection, kinematical criteria can be applied, such as requiring back-to-back events in the transverse plane, or a balance between the p_{T} vectors of the two muons. This last set of criteria can be used to reduce the background contribution from $t\bar{t}$ events; when they are not part of the pair selection, they are at least used to cross-check the results. The tag muon is required to pass the full Run 2 high- p_{T} ID described in section 4.3. After applying the probe selection, which depends on the efficiency under study, no further background subtraction is needed; the efficiency is calculated by counting passing and failing probe muons.

5.1 High- p_{T} muon identification efficiency

The Run 2 high- p_{T} ID efficiency is measured using the extended tag-and-probe method on muons that are reconstructed as global muons. The results are presented in figure 4 for the combined 2016 and 2017 data sets and for simulated DY samples. The efficiency as a function of p_{T} is shown separately in four η regions with different detector composition and characteristics: $|\eta| < 0.9$, only composed of DTs; $0.9 < |\eta| < 1.2$, composed of both DTs and CSCs; $1.2 < |\eta| < 2.1$, only composed of CSCs; and $2.1 < |\eta| < 2.4$, the very forward region composed of CSCs but very sensitive to pileup, punch through, and showering.

A very high identification efficiency, mostly above 98%, is found over the full detector acceptance. No p_{T} -dependent inefficiency is found for either 2016 or 2017 data. The DY simulation predicts slightly higher efficiency than observed in data, but the data-to-simulation agreement is uniform with increasing p_{T} . The “ $N - 1$ efficiencies” for each ID requirement are individually tested by dividing the number of probe muons passing a given selection criterion by the number of probe muons passing all other criteria. Figure 5 shows the results for each criterion that are obtained for

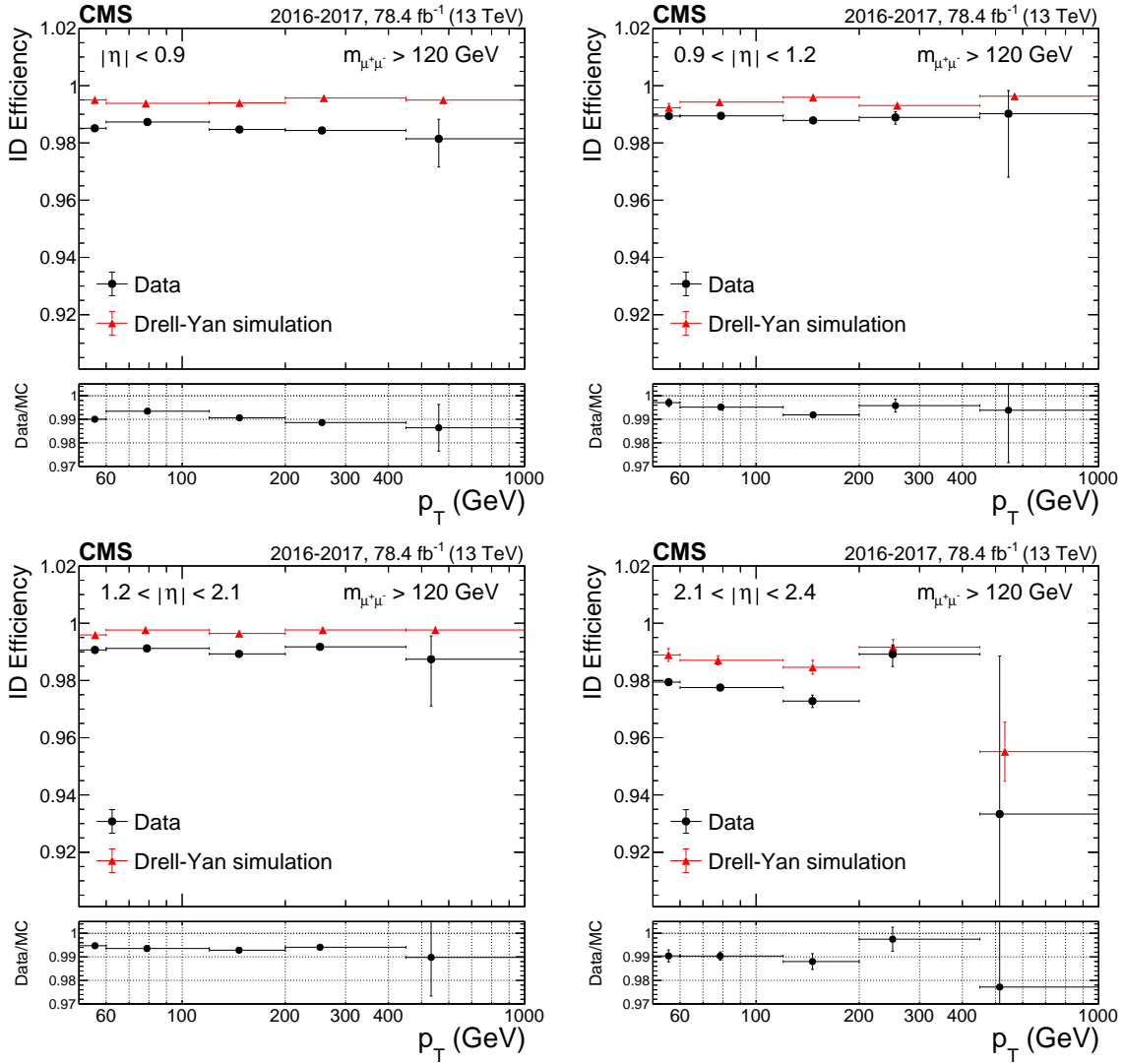


Figure 4. High- p_T ID efficiency for 2016 and 2017 data, and corresponding DY simulation, as a function of p_T for (upper left) $|\eta| < 0.9$, (upper right) $0.9 < |\eta| < 1.2$, (lower left) $1.2 < |\eta| < 2.1$, and (lower right) $2.1 < |\eta| < 2.4$. The black circles represent data; the red triangles represent DY simulation. The data-to-simulation ratio, also called the data-to-simulation scale factor (SF), is displayed in the lower panels. The central value in each bin is obtained from the average of the distribution within the bin.

muon $p_T > 53$ GeV and binned in η . Although the matching criteria between the muon system segments and the inner tracker part of the global muon were updated between Run 1 and Run 2 (section 4.3), this selection is still responsible for the slight discrepancy between simulation and data in the barrel region. In the endcaps ($|\eta| > 1.2$), we observe a slight inefficiency in both 2016 and 2017 data with respect to the rest of the detector and to simulation, due to the requirement of a valid muon detector hit in the final momentum fit. Finally, we observe a small efficiency gain in 2017 (+0.5%) with respect to 2016 in the barrel region, which can be traced back to the tracker part of the muon Run 2 high- p_T ID that links the improvement with the new pixel detector installed in CMS between the 2016 and 2017 data taking periods.

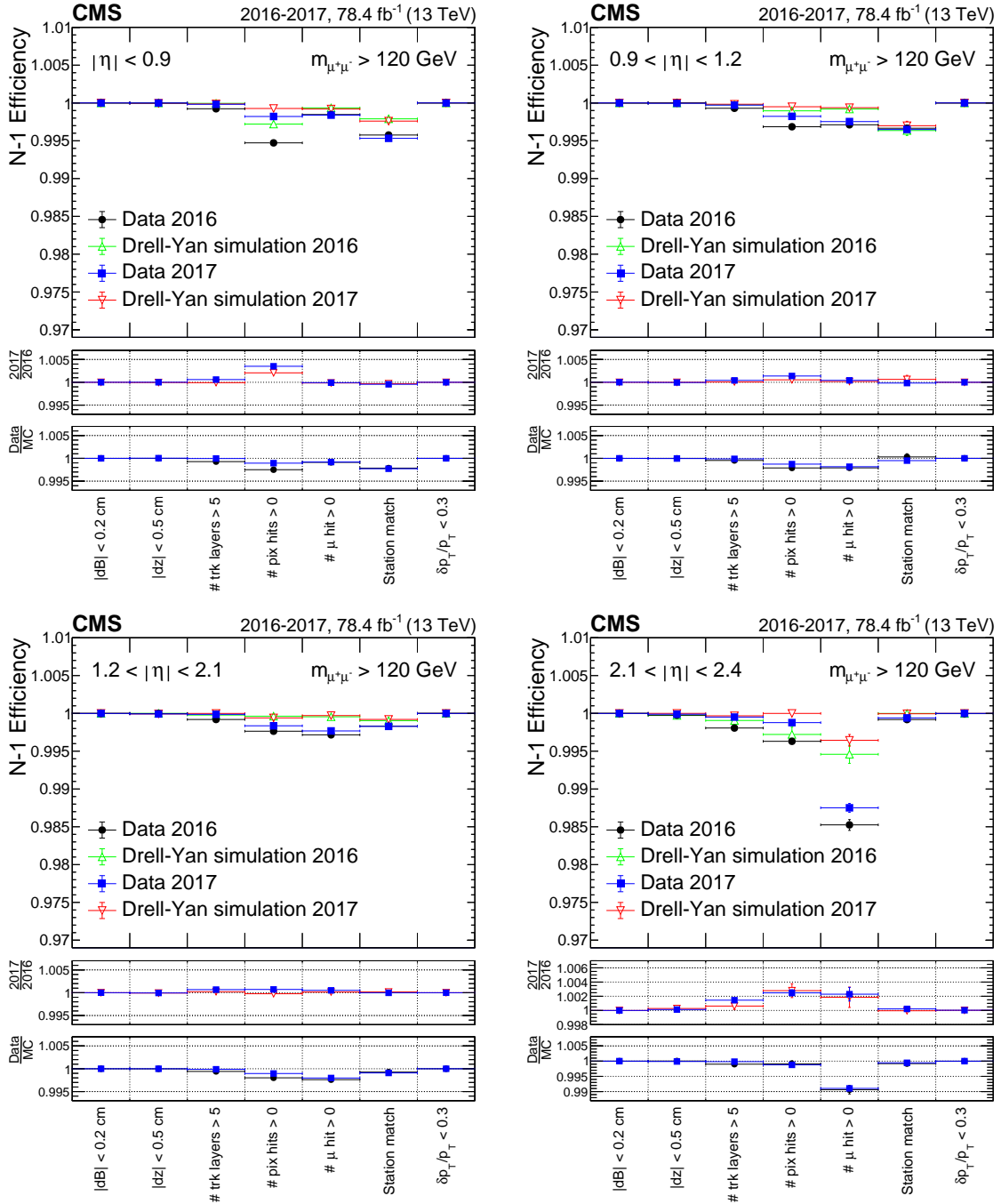


Figure 5. The $N - 1$ efficiencies, for $p_T > 53$ GeV and binned in η , comparison between 2016 and 2017 data sets and for the corresponding DY simulations, for (upper left) $|\eta| < 0.9$, (upper right) $0.9 < |\eta| < 1.2$, (lower left) $1.2 < |\eta| < 2.1$, and (lower right) $2.1 < |\eta| < 2.4$. The black circles represent 2016 data; the blue squares represent 2017 data. The lower panels display the ratio of $N - 1$ efficiencies obtained for each of the criteria, between 2017 and 2016 data sets, and between data and their corresponding simulations for both years.

The Run 2 high- p_T ID efficiency is very high and no trend is observed with increasing p_T . The results are also provided as a function of the muon p in figure 6. The 2016 and 2017 data sets are combined in order to reach higher sensitivity. The efficiencies are further split into two categories, whether or not a shower is tagged, given a muon. The overlap region ($0.9 < |\eta| < 1.2$) is not included, to avoid double counting from CSC and DT segment-overlap that biases the shower tagging definition. No effect due to showering can be seen in the endcap region (upper right and lower plots), but a slight decrease in the efficiency of 1% is visible over the full momentum spectrum in the barrel region (left plot) for muons with an associated shower. This inefficiency is due to requirements on the matching of the inner track to the segments in the muon system, which are responsible for most of the inefficiency in the barrel region. In most of the cases, the muon is failing these identification criteria because it fails to be reconstructed as a tracker muon, despite the fact that the global reconstruction is successful. It appears likely that those muons are emitting showers in the calorimeters, which cause a change in trajectory before entering the muon system, so that the tracker-track extrapolation does not match the segments.

5.2 Reconstruction efficiency

The standalone and global muon reconstruction efficiencies are studied as a function of muon η and p using the extended tag-and-probe method. The selected probe muons are required to be good quality tracker muons, and the efficiency to reconstruct either standalone or global muons is calculated with respect to these probes. Figure 7 shows the 2016 and 2017 standalone muon reconstruction efficiency as a function of muon η for muons with $p_T > 53$ GeV. The efficiency is above 99% in the barrel region and up to $|\eta| = 1.6$, both for data and simulation, and for both data sets. For $|\eta| > 1.6$, the simulation does not reproduce the slight inefficiency observed in data.

To characterize the inefficiency seen in the forward part of the detector and in both data sets, figure 8 shows the standalone muon reconstruction efficiency as a function of p for $|\eta| < 1.6$ and for the forward endcaps ($1.6 < |\eta| < 2.4$). The measured efficiency in the $|\eta| < 1.6$ region is uniform in p up to approximately 2 TeV in both data and simulation. In the region $1.6 < |\eta| < 2.4$, a decreasing trend as a function of p is observed in both data and simulation, although it is more pronounced in data by approximately 2%. In order to separate out the possible effect of pileup (in particular since the forward part of the detector suffers from the dense track activity), figure 9 compares the standalone reconstruction efficiency obtained in data with DY simulation for events with low pileup environment (defined as having less than 15 reconstructed primary vertices) and for events with higher pileup environment. In addition, since the muons crossing the forward region of the detector have a higher probability to shower (figure 2), the results are then further split between events where at least one shower is tagged from events without any showering detected.

For the low-pileup environment and events without tagged showers, the efficiency measured both in simulation and in data is mostly uniform across the momentum spectrum and is almost 100 (99)% in simulation (data). It starts to show a decreasing trend for higher pileup activity with the efficiency going down to 98 (96)% for muons with momentum of a few TeV in simulation (data). Although the simulation results show a dependence on the level of pileup, they do not reproduce the data trend when there are more than 15 vertices. When no shower is found, the decreasing trend seen in simulation, and more pronounced in data, is due to pileup. In the presence of showers, the inefficiency trend is enhanced in both data and simulation, and in particular for events inside

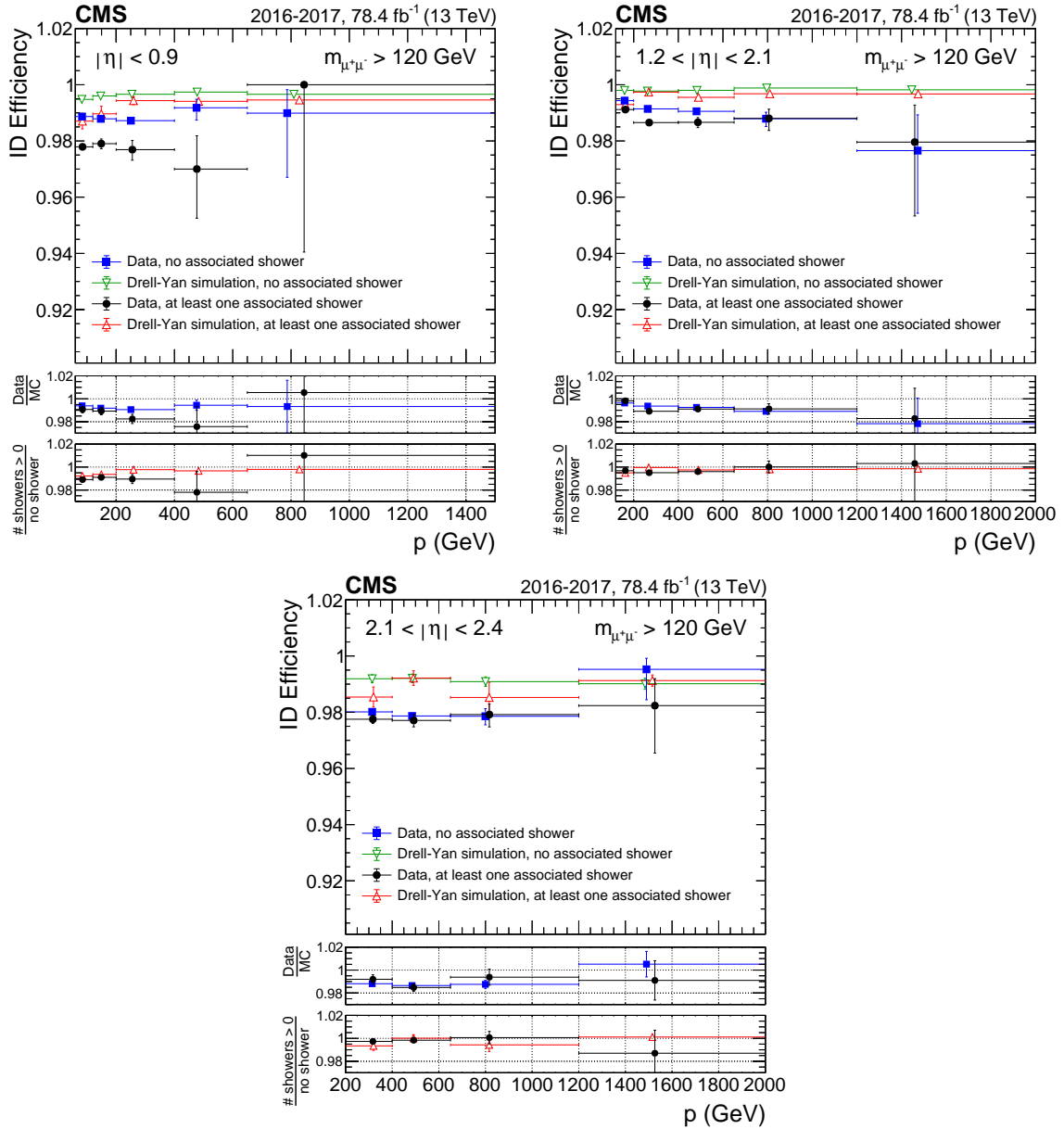


Figure 6. High- p_T ID efficiency for 2016+2017 data, and corresponding DY simulation, as a function of p for (upper left) $|\eta| < 0.9$, (upper right) $1.2 < |\eta| < 2.1$, and (lower) $2.1 < |\eta| < 2.4$. The blue squares show efficiency for muons in data with no showers tagged; the green inverted triangles show the same for muons in DY simulation. The black circles correspond to muons in data with at least one shower tag, while the red triangles are the same for muons in DY simulation. The central value in each bin is obtained from the average of the distribution within the bin.

the high pileup environment, where the lowest efficiency value is 95 (93)% for muons of few TeV in simulation (data). The data vs. simulation discrepancy is slightly enhanced in the presence of showering for events recorded in both low- and high-pileup environments. We conclude that muon showering and dense track activity interfere within the muon reconstruction, and lead to the momentum dependence of up to 5% in the inefficiency when both effects are combined.

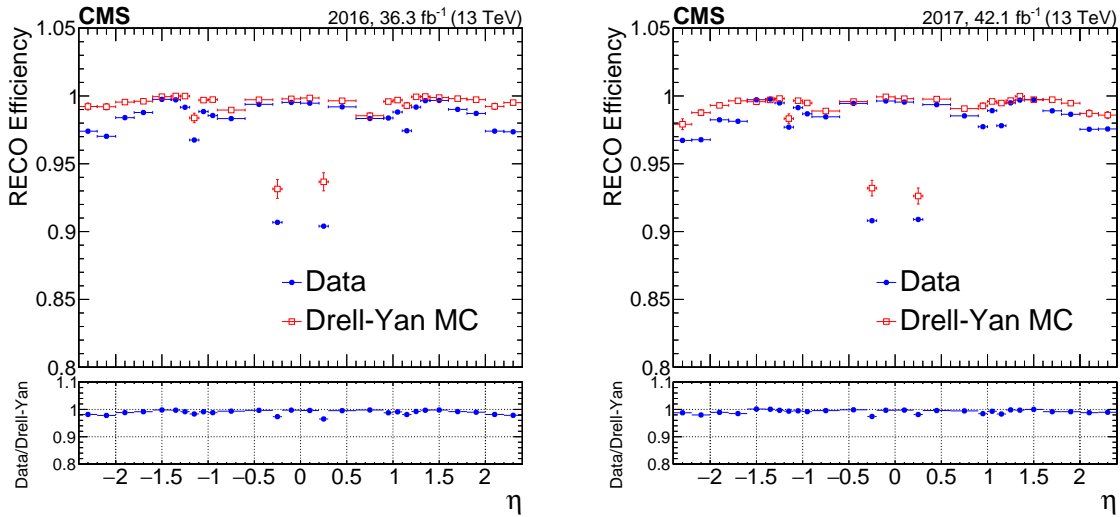


Figure 7. Standalone muon reconstruction efficiency as a function of muon η for the (left) 2016 and (right) 2017 data sets. The blue points represent the data, while the red empty squares represent the simulation.

The scrutiny of DY events from simulation shows that approximately half of the events responsible for the reconstruction inefficiency do have a standalone muon, but it is not associated with its tracker part. Despite the fact that the tracker part and the standalone muon share common segments, the extrapolation of the standalone muon to the tracker volume is not succeeding. Hence the standalone muon and the global muon formed from it (if any) both exist, but the momentum assignment is wrong. The other half of the events are again good tracker muons, with associated muon segments in several muon chambers, but in these cases no standalone muon is reconstructed. Still, several segments are found across the entire muon system (over the 4 stations) and they match the tracker part. This observation indicates a reconstruction failure at the muon system level, namely the inability to reconstruct the standalone trajectory out of the detected segments.

The global reconstruction efficiency is computed for probe muons that are also standalone muons and is displayed as a function of the muon momentum in figure 10. The results are integrated over muon η but split according to the (left) absence or (right) presence of showers. The efficiency is almost 100% over the full momentum spectrum when the events do not contain showering muons. A slight decreasing trend is observed in the presence of muon showering, although the global reconstruction efficiency remains greater than 99%.

5.3 Combined L1 and HLT efficiency

The overall trigger efficiency (combined L1 and HLT) is measured using the extended tag-and-probe method, as well as using events selected by a set of triggers without muon requirements. The events selected in these independent data sets contain a high-energy electron or large p_T^{miss} . This second approach leads to a sample enriched in W +jets and $t\bar{t}$ events that could be used to probe muon triggers.

Figure 11 shows the trigger efficiency measurement using the extended tag-and-probe (black), and independent data set (red) methods as a function of the muon p_T for 2016 and 2017 data. The

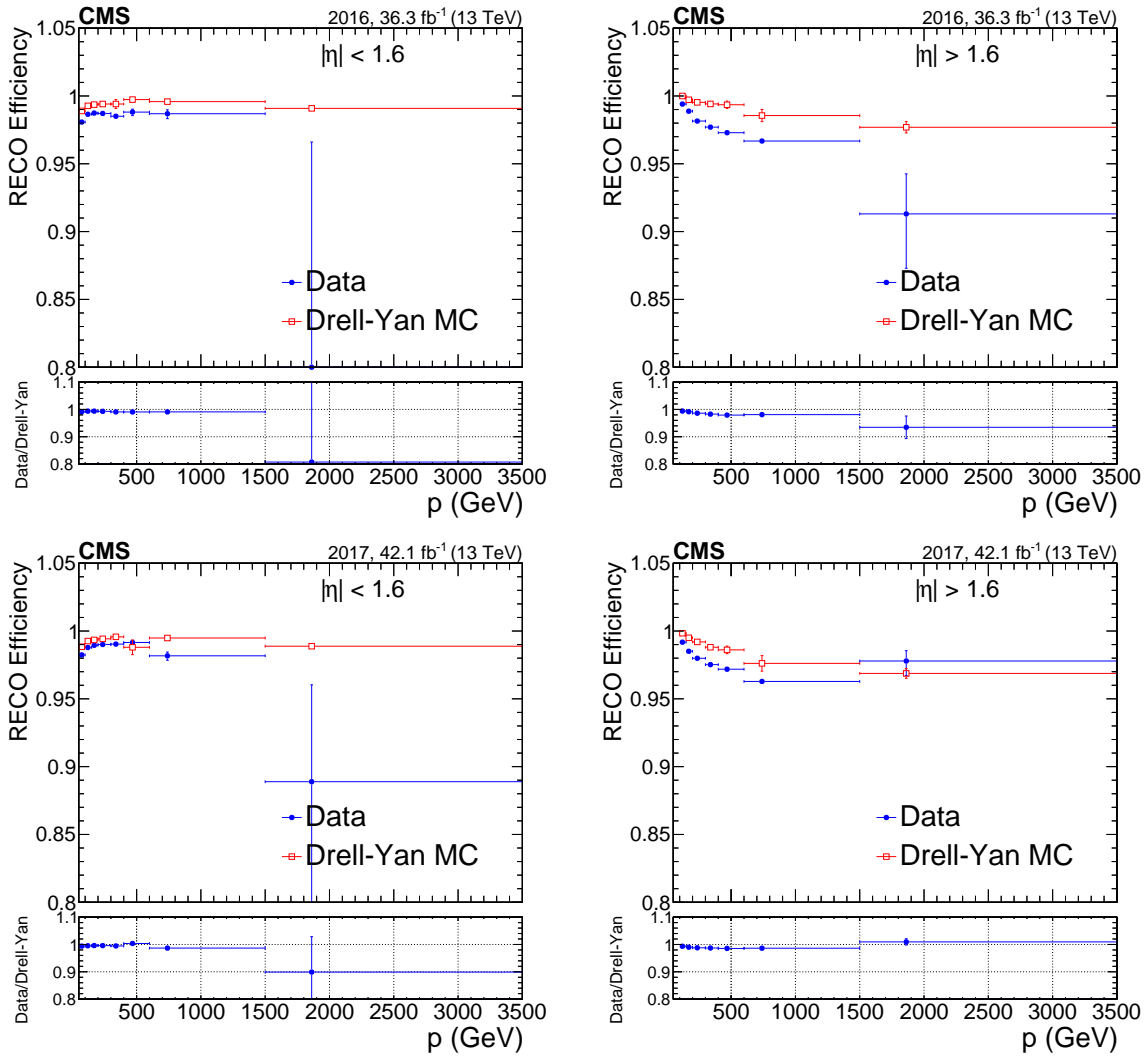


Figure 8. Standalone muon reconstruction efficiency as a function of muon momentum in two different $|\eta|$ regions: (left) $|\eta| < 1.6$, and (right) forward endcaps from, $1.6 < |\eta| < 2.4$. The upper row shows the 2016 results, with blue points representing data and red empty squares representing simulation. The lower row shows the 2017 results. The lower panels of the plots show the ratio of data to simulation. The central value in each bin is obtained from the average of the distribution within the bin.

two methods are compatible with each other, reinforcing the robustness of the results. The measured trigger efficiency in 2016 and 2017 data shows a slight decreasing trend as a function of the muon p_T with a value of 90 (85)% at 60 GeV (1 TeV). The SF between the trigger efficiencies in data and simulation ranges between 0.95 and 0.9.

The 2016 and 2017 trigger efficiencies obtained with the extended tag-and-probe method are computed separately for the barrel and overlap regions, and compared to simulation in figure 12. In both data sets, the efficiency trend as a function of p_T is seen in the barrel but even more pronounced in the overlap region. In the barrel, the ratio of data to simulation is 0.98 (0.97) for 2016 (2017) data and is uniform with p_T in both data sets. The residual efficiency dependence of the results is caused by the L1 component, due to the lower efficiency of the L1 muon trigger for muons with shower

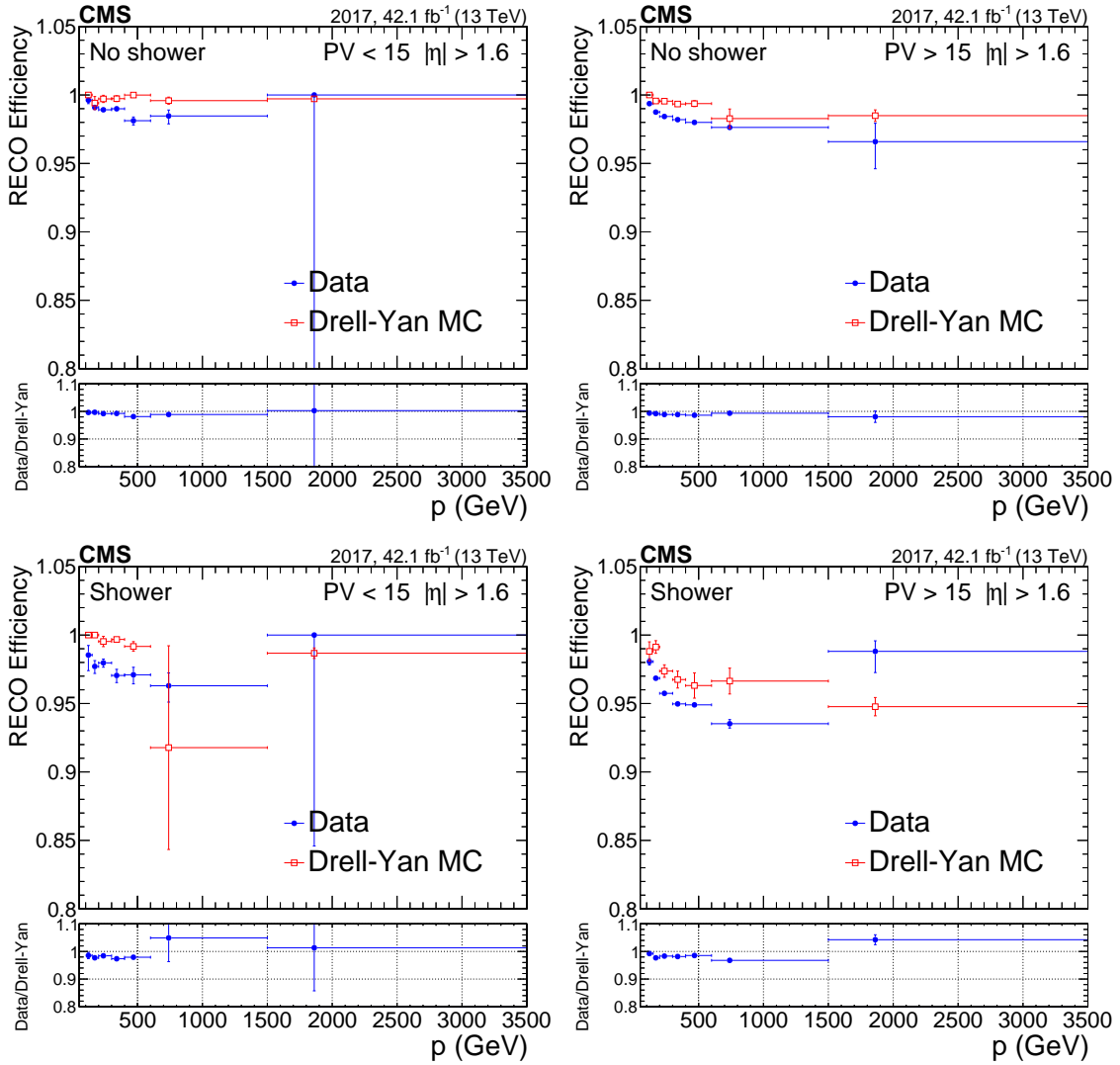


Figure 9. Standalone muon reconstruction efficiency as a function of muon p for muons with $1.6 < |\eta| < 2.4$. The left plots are for low pileup (up to 15 vertices) while the right plots are for higher pileup. The upper plots are obtained with events without any showers; the lower ones contain events with at least one shower. The blue points represent data and the red empty squares represent simulation. The lower panels of the plots show the ratio of data to simulation. The central value in each bin is obtained from the average of the distribution within the bin.

tags, as discussed in section 5.4. In the overlap region, the inefficiency trend is much more severe in data than in simulation, and the SF are increasing with p_T . They range from 0.95 at 60 GeV and down to 0.85 GeV in the highest bin in 2016 data (and 0.9 in 2017 data). Hence, though the efficiency trend is visible in both the barrel and overlap regions, the p_T dependence of the SF is coming exclusively from the overlap region. This effect has been tracked down to the L1 trigger and the causes are attributed to a nonoptimal arbitration between the DT and CSC segments that are both present in the overlap region. Even though the muon identification relies equally on CSC and on DT segments, the momentum assignment will be more accurate if the estimated value comes

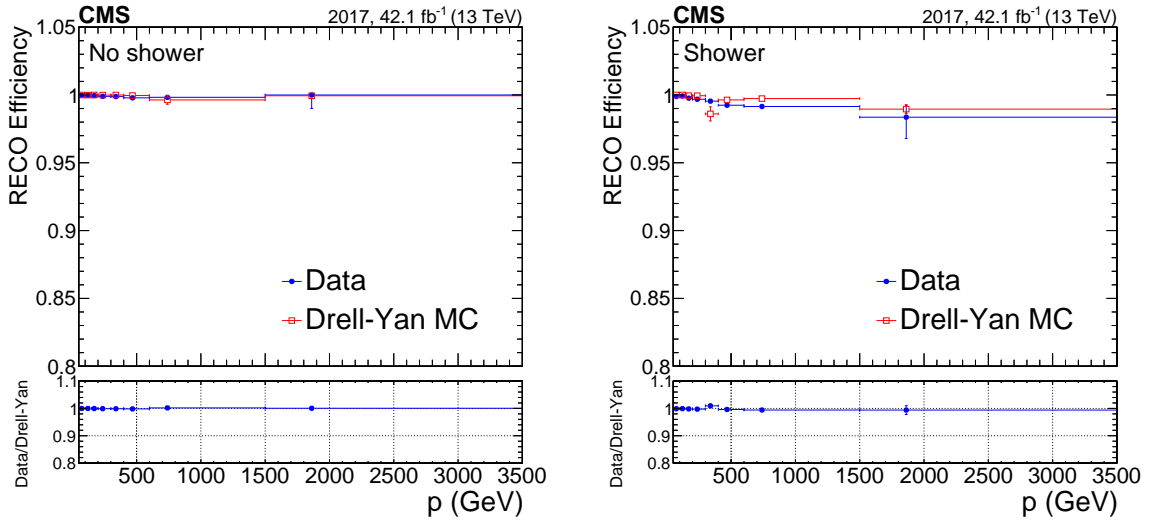


Figure 10. Global muon reconstruction efficiency as a function of muon momentum. The left plot is obtained with events without any showers, while the right one contains events with at least one shower. The blue points represent data and the red empty squares represent simulation. The lower panels of the plots show the ratio of data to simulation. The central value in each bin is obtained from the average of the distribution within the bin.

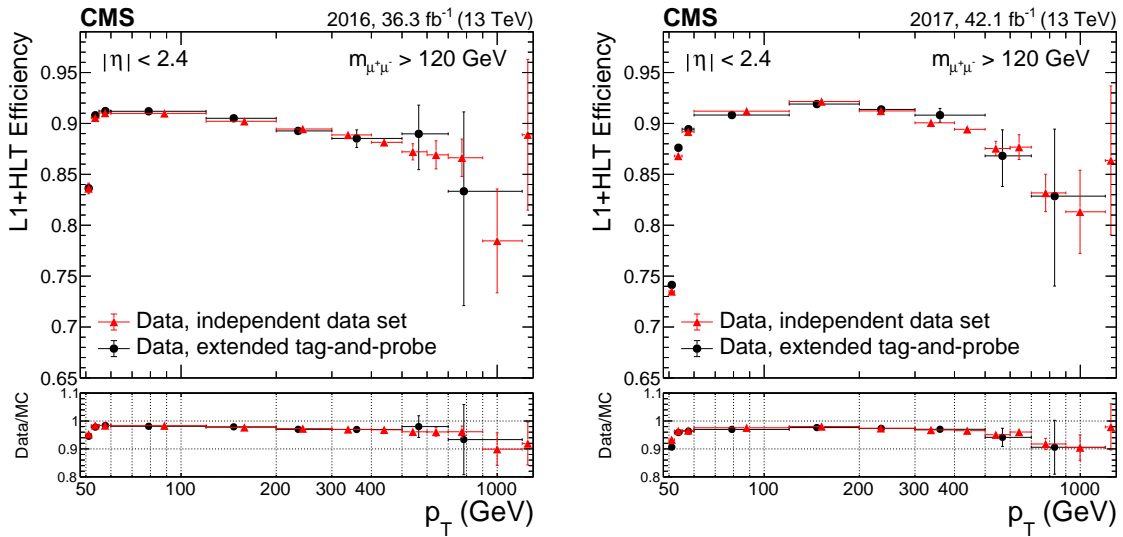


Figure 11. The combined HLT+L1 efficiency with respect to the offline selection, and the ratio of data to simulation for different methods, as functions of p_T , for (left) 2016 data and (right) 2017 data. The red triangles are measured using an independent data set collected with a p_T^{miss} trigger; the black circles are measured by the extended tag-and-probe method in which selected events have $m_{\mu\mu} > 120$ GeV. The central value in each bin is obtained from the average of the distribution within the bin.

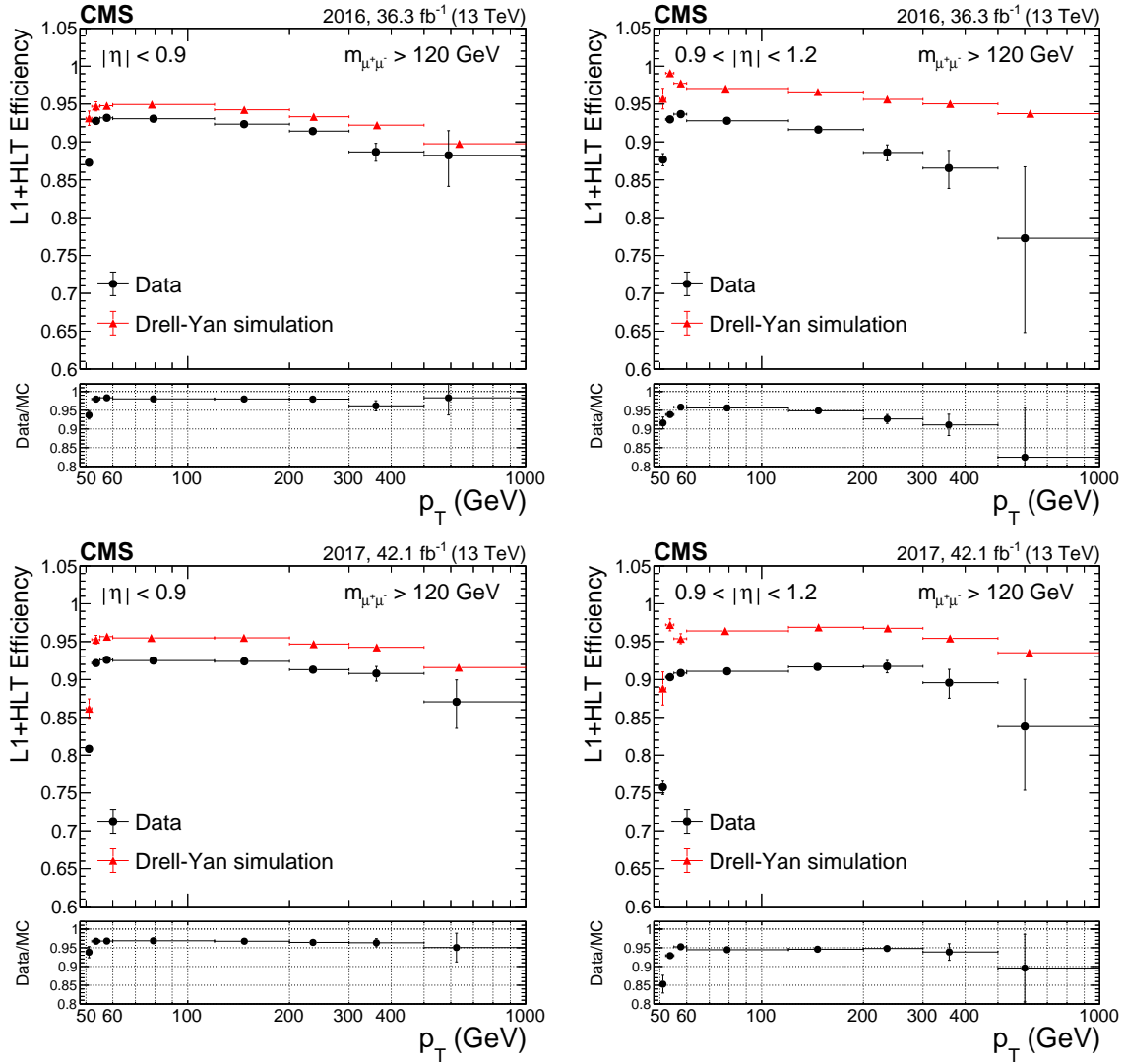


Figure 12. The combined HLT+L1 efficiency with respect to the offline selection, and the ratio of data to simulation, as a function of p_T , for (upper) 2016 data and (lower) 2017 data and simulation. The left plots are for the barrel region and the right plots are for the overlap region. The red triangles represent the simulation while the black dots are the data. The lower panels display the ratio of efficiencies in data and simulation. The central value in each bin is obtained from the average of the distribution within the bin.

from the DT. A fix was implemented in 2018 so that the DT estimated muon assignment is used in these cases.

5.4 The L1 trigger efficiency

The L1 component of the overall muon trigger efficiency at high p_T is parameterized separately for the two cases when an associated shower is, or is not, tagged. From figure 11, it can be seen that above the initial turn-on curve, the trigger efficiency is mostly uniform, but appears to be slowly deteriorating as the muon momentum increases. It is important to quantify the size of this effect from L1, because it can impact all high- p_T physics measurements.

The approach used here relies on assuming that the inefficiency appearing at high p_T is due to showering in the muon detectors, and that the momentum dependence arises because the probability of showering in a station increases with increasing momentum. That is, the efficiency under study can be parameterized as a function of the number of showers $\epsilon(N_{\text{shower}})$, which should be independent of the momentum.

The validity of the shower-based approach is verified by studying the L1 muon efficiency as a function of the number of showers for different muon momentum slices. We observe that, within a momentum slice, the trigger efficiency does correlate with the number of showers. Furthermore, the dependence on N_{shower} is the same or similar across the compared p ranges.

The shower probability shown in figure 2 is parameterized as a function of muon momentum as $P_{\text{shower}}(p)$. The parameterization is performed by fitting the distribution in the region up to 1 TeV, separately for the data and for the DY simulation, with a linear function. The upper end of the range is dictated by the lack of a sufficient number of muons in data above $p \approx 1$ TeV.

The L1 efficiency can thus be calculated as a function of p according to:

$$\epsilon_{\text{L1}}(p) = \sum_{N_{\text{shower}}=0}^4 \epsilon(N_{\text{shower}}) P_{N_{\text{shower}}}(p), \quad (5.2)$$

where $P_{N_{\text{shower}}}(p)$ is the probability for a muon of momentum p to produce the number of showers given by N_{shower} , which can be calculated from $P_{\text{shower}}(p)$ using standard combinatorial formulas. The maximum number of showers is 4 since there are 4 muon stations.

We extract $\epsilon(N_{\text{shower}})$ from simulated DY events and from the 2016 and 2017 data sets recorded with the p_T^{miss} trigger. An event selection is applied to remove cosmic ray muons from the data and to select only well-reconstructed isolated muons passing the high- p_T identification criteria. Regions in the barrel ($|\eta| < 0.9$) and endcap ($|\eta| > 1.2$) are analyzed separately. The overlap region where muons can have hits in both DT and CSC is not considered in this study.

For each muon reconstructed offline, the L1 muon candidates close to the extrapolated muon trajectory are stored. The candidate with the highest p_T and in time with the collision is taken as the L1 candidate assigned to this muon. The L1 efficiency for the muon is defined based on whether an L1 candidate with p_T above the L1 threshold (22 GeV) is found or not.

The final efficiency measurement is extracted from a combination of 2016 and 2017 data sets, which maximizes the sample size. The resulting L1 efficiency for muons with different numbers of showers is shown in table 1.

These numbers are combined with the parameterization of the number of showers versus p , as described above, yielding the L1 efficiency, as a function of p , shown in figure 13. The results shown as a black line in the plot were derived using the shower-based approach described above, taking both the shower probability and the L1 efficiency from data. The shaded bands represent the statistical and systematic uncertainties of the shower probability determination. They are dominated by the small number of events at high momentum, particularly in the barrel region (cf. figure 2). The efficiency calculated directly from the data events is shown as black points. The two methods give comparable results, indicating that the presence of showers contributes to the L1 inefficiency at high momentum. The L1 efficiency measured in the simulated DY sample is shown for comparison, as blue points and lines. The two methods agree well, with a decreasing efficiency trend similar to that observed in data.

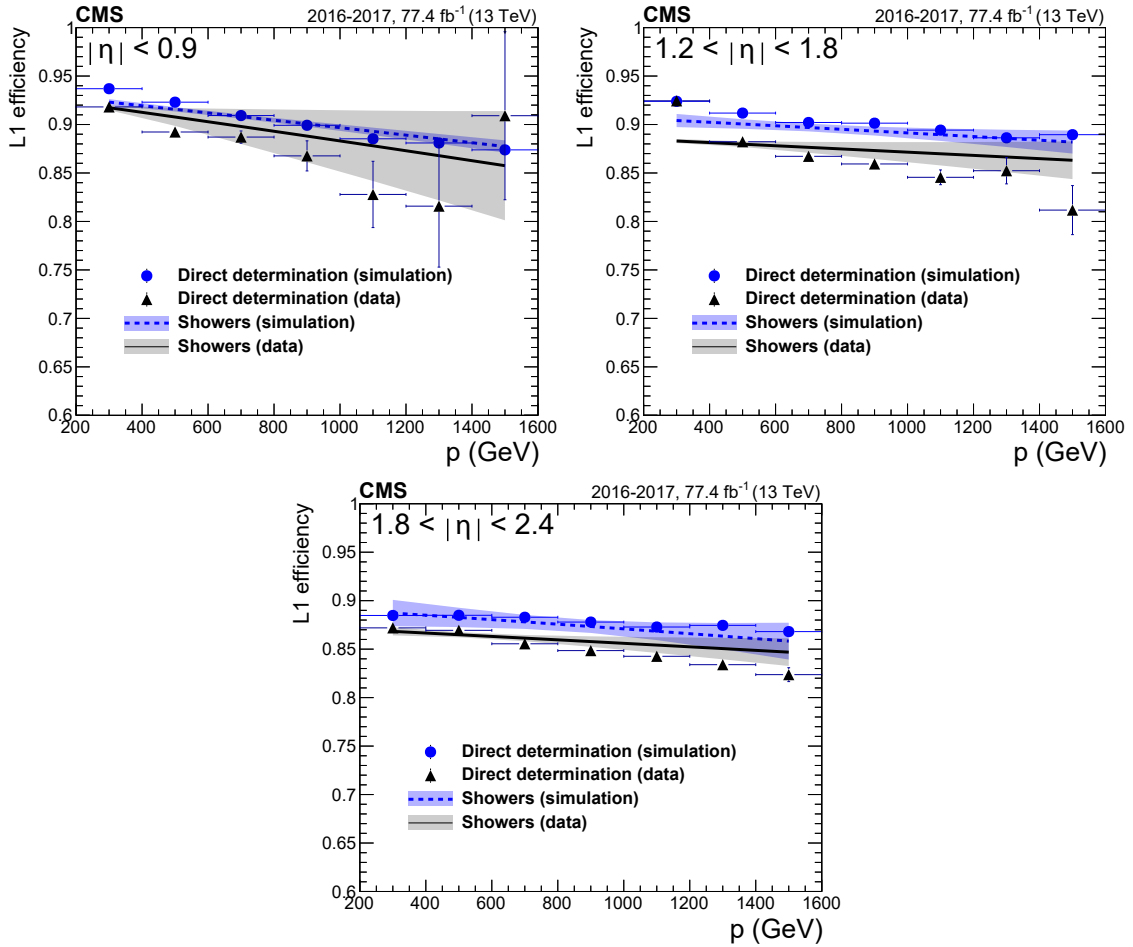


Figure 13. The L1 efficiency in three η regions: (upper left) barrel; (upper right) for muon with $1.2 < |\eta| < 1.8$; and (lower) endcap with muon $|\eta| > 1.8$. The plots show a comparison between directly determining the efficiency from simulation (blue dots) and with data (black triangles) with respect to calculating it from shower multiplicity, both in 2016+2017 combined data (black line) and 2017 simulation (dashed blue line). The shaded bands include the statistical uncertainties of the measurements and the systematic uncertainty of the showering probability determination.

Table 1. The L1 trigger efficiency for barrel and endcap muons measured as a function of the number of showers in the muon stations. The endcap was split into near ($|\eta| < 1.8$) and far ($|\eta| > 1.8$) sections.

N_{shower}	Barrel L1 efficiency		Near endcap L1 efficiency		Far endcap L1 efficiency	
	Data	Simulation	Data	Simulation	Data	Simulation
0	$93.9 \pm 0.1\%$	$94.4 \pm 0.1\%$	$89.3 \pm 0.1\%$	$91.4 \pm 0.1\%$	$88.3 \pm 0.1\%$	$90.0 \pm 0.1\%$
1	$82.2 \pm 0.1\%$	$82.7 \pm 0.1\%$	$84.9 \pm 0.2\%$	$87.2 \pm 0.1\%$	$83.5 \pm 0.1\%$	$85.9 \pm 0.1\%$
2	$67.1 \pm 0.7\%$	$67.3 \pm 0.3\%$	$78.9 \pm 0.5\%$	$81.9 \pm 0.3\%$	$77.0 \pm 0.2\%$	$79.8 \pm 0.3\%$
3	$49.8 \pm 3.4\%$	$50.1 \pm 1.4\%$	$76.9 \pm 2.0\%$	$76.0 \pm 1.0\%$	$70.2 \pm 0.8\%$	$72.7 \pm 0.9\%$
4	$40 \pm 15\%$	$36 \pm 9\%$	$68 \pm 11\%$	$75 \pm 5\%$	$63 \pm 3\%$	$60 \pm 4\%$

6 Momentum assignment performance

At low and intermediate momenta, below 100 GeV, the muon p_T resolution is dominated by the hits measured in the silicon tracker. In contrast, hits and segments measured in the muon chambers are significantly affected by multiple scattering of the muon trajectory while passing through the calorimeters and the flux-return yoke. This multiple scattering is reduced with increasing momentum, and above 200 GeV the muon chamber measurements start to improve on the measured p_T . The ultimate performance at high p_T is then determined by the precision of the muon chamber measurements and by the alignment of muon chambers relative to each other and to the inner tracker.

The alignment of the silicon tracker is a challenging task, achieving a statistical accuracy better than $10\ \mu\text{m}$ on the position of individual detector modules [26, 27]. To these small remaining alignment uncertainties one has to add the intrinsic resolution of silicon hits (typical $10\text{--}30\ \mu\text{m}$). The intrinsic precision of the muon DT chambers in the barrel region and the CSC in the endcap region, is of the order of $100\text{--}200\ \mu\text{m}$, to which the possible chamber misalignment is added in quadrature [4].

Until 2015, the CMS muon reconstruction neglected the alignment uncertainties of the muon chambers, referred to as alignment position errors (APE). Resultant shortcomings were evident, as observed deviations were larger than expected uncertainties for the muon segment parameters with respect to the extrapolated track from the inner tracker. The best possible reconstruction for a high- p_T muon track can be reached by a correct relative weighting of tracker and muon detector hits. In the high-momentum regime this balance requires including appropriate muon alignment uncertainties in the Kalman filter. From the beginning of Run 2, the muon reconstruction has been using nonzero muon APEs [28]. Muon APEs have been introduced for local reconstructed segments in each station for all six segment degrees of freedom (three local positions x , y , and z ; and three local angles ϕ_x , ϕ_y , and ϕ_z), chamber-by-chamber, for both DT and CSC chambers; they are taken as uncorrelated, as a first approximation.

The muon momentum resolution and the closely related charge assignment are studied in detail using simulation in section 6.1. These studies span the entire momentum spectrum with high precision and provide estimates of the impact of different detector alignment conditions, with and without the APEs. The performance of the momentum resolution and scale measurements are then assessed in data from both cosmic ray muons and collisions, and compared to simulation, in sections 6.2 and 6.3, respectively.

6.1 Momentum performance in simulation

The momentum resolution of highly energetic muons can be measured in simulated events, where the true muon momentum is known. The resolution can be extracted from the distribution of the relative residual in q/p :

$$R_{\text{reco-gen}} = \frac{(q/p)^{\text{reco}} - (q/p)^{\text{gen}}}{(q/p)^{\text{gen}}}, \quad (6.1)$$

where q/p is the charge sign divided by the momentum of the muon. The expectations for various alignment scenarios have been tested in simulation on back-to-back dimuons with distributions uniform in η , ϕ , and p , within the range $5\ \text{GeV} < p < 2.5\ \text{TeV}$. For smaller intervals of momentum within that range, the standard deviation σ of a fit to a Gaussian function of the distribution for the

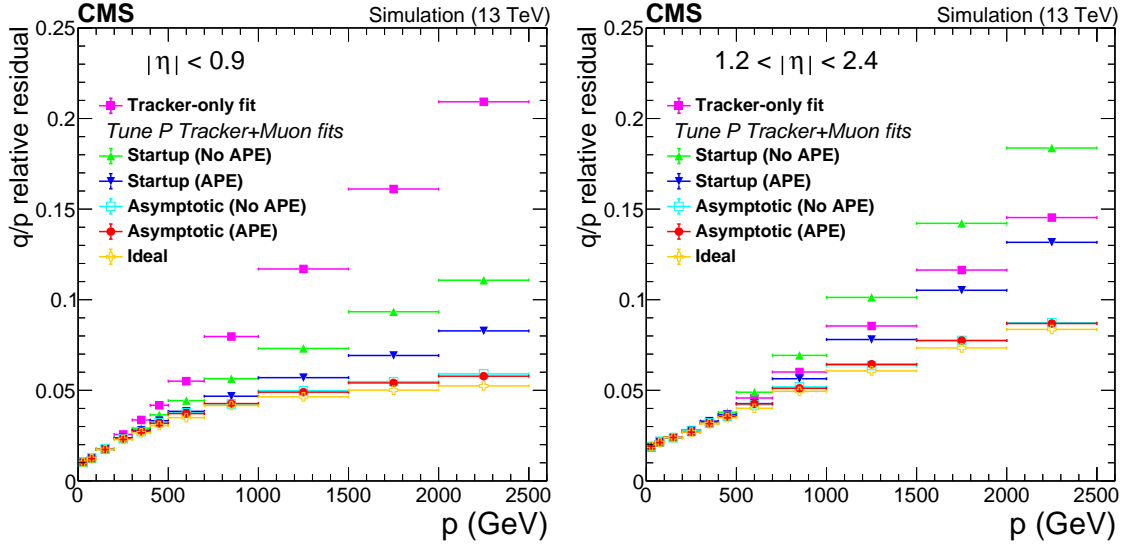


Figure 14. Muon momentum resolution (standard deviation σ of the fit of the core distributions to a Gaussian function) in (left) the barrel region $|\eta| < 0.9$ and (right) the endcap region $1.2 < |\eta| < 2.4$, for the TuneP algorithm, as a function of muon momentum, for the various misalignment scenarios with and without APEs. A comparison with the ideal scenario is also given. The performance of the tracker-only fit is shown for comparison.

TuneP algorithm is shown in figure 14, as a function of the momentum. The performance of the tracker-only fit is also given for comparison.

Startup and asymptotic scenarios with and without the corresponding APEs have been simulated, together with the ideal scenario with no misalignment (APEs set to zero). The startup scenario corresponds to the preliminary alignment at the beginning of a data-taking period. The startup performance is expected to be suboptimal, in particular because of alignment after the opening and closure of the detector during the LHC shutdown periods. The final alignment of the individual muon chambers (both DT and CSC), also called asymptotic, is determined starting from the aligned silicon tracker geometry, by extrapolating selected muon tracks from the inner tracker to the muon chambers [29]. The alignment algorithm can use both cosmic ray muons and muons from pp collisions, selected with high purity and p_T above a minimum threshold to limit the multiple scattering ($p_T > 30$ GeV for collision muons in 2016 data taking). Significant improvements are found with the inclusion of APEs in the startup scenario. In the endcaps, the startup performance is worse than tracker-only, but gets recovered with APEs. In the barrel region, the performance gets closer to asymptotic by including the APEs. Overall, there are also small improvements for the asymptotic scenario due to the inclusion of APEs.

To further assess the performance of the TuneP algorithm, it is important to study not only the Gaussian core resolution, but also the tails of the residual distribution that are sensitive to muon showering. We characterize the tails by the fraction of muons with relative momentum residual $|\delta k/k| > 20\%$ (with $k = q/p$), as a function of the muon momentum. The comparisons of the momentum resolution and the tails between the global muon fit and the TuneP choice are shown in figure 15 for the asymptotic conditions of alignment and APEs. Two cases are defined by whether or not at least one shower was found in the muon system.

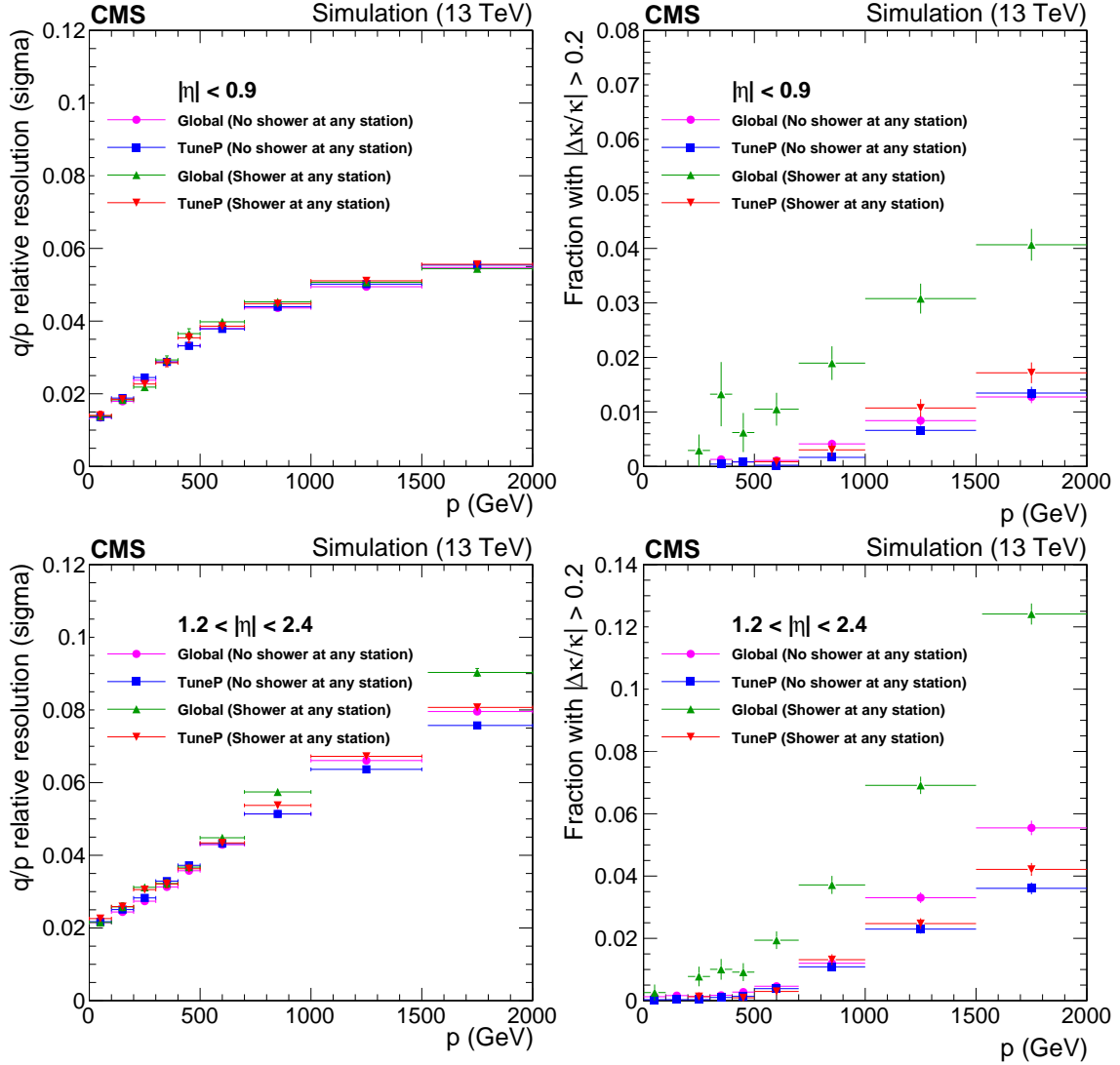


Figure 15. Comparison of the TuneP and global reconstruction algorithms for simulated muons in the (upper) barrel and (lower) endcap, for the cases with and without the presence of tagged showers in any muon station. The left plots show the momentum resolution (Gaussian σ); the right plots show the tail fraction with $|\delta k/k| > 20\%$, as a function of muon momentum.

With TuneP, the momentum resolution σ is about 2% for muons with $p < 200$ GeV in the barrel, whereas it is slightly above that value in the endcap. At 2 TeV, the resolution reaches about 6% in the barrel and 8% in the endcap. A clear advantage of the strategy to remove contaminated muon stations from the trajectory fit is seen by comparing the resolution tails of the global muon fit and TuneP. The TuneP p_T assignment is mostly independent of showering. This does not come at the expense of the core resolution, which does not degrade with respect to the global muon fit, but rather is also slightly improved.

Finally, the TuneP momentum assignment provides a reliable determination of the muon charge sign up to very high momenta. Several studies made on DY and single muon simulations predict a charge misassignment probability varying from 10^{-5} to 10^{-4} for muon momenta from 100 GeV

to 2 TeV. Cosmic ray muons can be used to partially validate these probabilities [30]. During Run 2, we collected 20 000 cosmic ray muons crossing the tracker volume of CMS with $p_T > 30$ GeV. Only one cosmic ray muon appears to have a wrong charge assignment, with apparent $p_T = 640$ GeV (estimated from the lower CMS hemisphere).

6.2 Momentum resolution from cosmic ray muons and collision events

In addition to the muons produced from heavy-boson decays, high- p_T muons from cosmic ray interactions and decays in the atmosphere [31] provide an excellent source of clean events that the CMS detector can measure. As the muons traverse the CMS detector close to vertically, two reconstructed legs (upper and lower) provide independent measurements of the momentum for a single physical muon. The muon momentum scale and resolution can then be assessed. For each selected event, we require two global muons, one in each hemisphere of the detector, with good tracker track quality to further ensure that the track is crossing well within the tracker volume, similarly to muons produced in pp collisions.

The two global muon tracks belong to the same cosmic ray muon trajectory and should then have similar momentum. It is then possible to extract the relative q/p_T residual, $R_{\text{cosmic}}(q/p_T)$, defined as:

$$R_{\text{cosmic}}(q/p_T) = \frac{(q/p_T)^{\text{Upper}} - (q/p_T)^{\text{Lower}}}{\sqrt{2}(q/p_T)^{\text{Lower}}}, \quad (6.2)$$

where $(q/p_T)^{\text{Upper}}$ and $(q/p_T)^{\text{Lower}}$ are the charge sign divided by p_T for the upper and the lower muon tracks, respectively. The factor of $\sqrt{2}$ accounts for the fact that the q/p_T measurements of the two tracks are independent.

Figure 16 compares the p_T resolution from R_{cosmic} measured with the cosmic ray muons collected in 2016 and 2017, crossing the barrel ($|\eta| < 1.2$) and the endcap ($1.2 < |\eta| < 1.6$) regions. The fits use the TuneP algorithm and the resolution obtained from simulated DY events, $R_{\text{reco-gen}}$, is defined in eq. (6.1). One third of the cosmic ray muon sample was collected during collisions using the same single-muon trigger used to record high-momentum muons from heavy-boson decays in order to guarantee the same detection environment; the remainder was collected during dedicated cosmic ray muon runs with no LHC beams. The full cosmic ray muon sample has the same reconstruction procedure as that used for pp collisions. Good agreement is found between the cosmic ray muon data and the simulated DY events. The uncertainties in the highest bins are dominated by the small number of cosmic ray muons recorded (only 247 events with $p_T > 500$ GeV).

The coverage in η is limited with cosmic ray muons, which are predominantly close to vertical. Hence the momentum resolution performance is measured best for $|\eta| < 1.6$. To overcome this limitation, events in the Z boson peak from pp collisions can be used to assess the dimuon mass resolution, as a function of the p_T of the individual muons in a dimuon pair. The mass resolution function is the convolution of a Breit-Wigner distribution that models the intrinsic decay width of the Z boson (both mean and width set to the PDG values [20]) with a double Crystal Ball function [32, 33] that models the detector effects. The Z boson peak is fit in a mass range $75 < m_{\mu\mu} < 105$ GeV. Each muon in the event is counted separately when filling the histograms, according to muon p_T , so that each event is counted twice. The resulting dimuon mass resolution

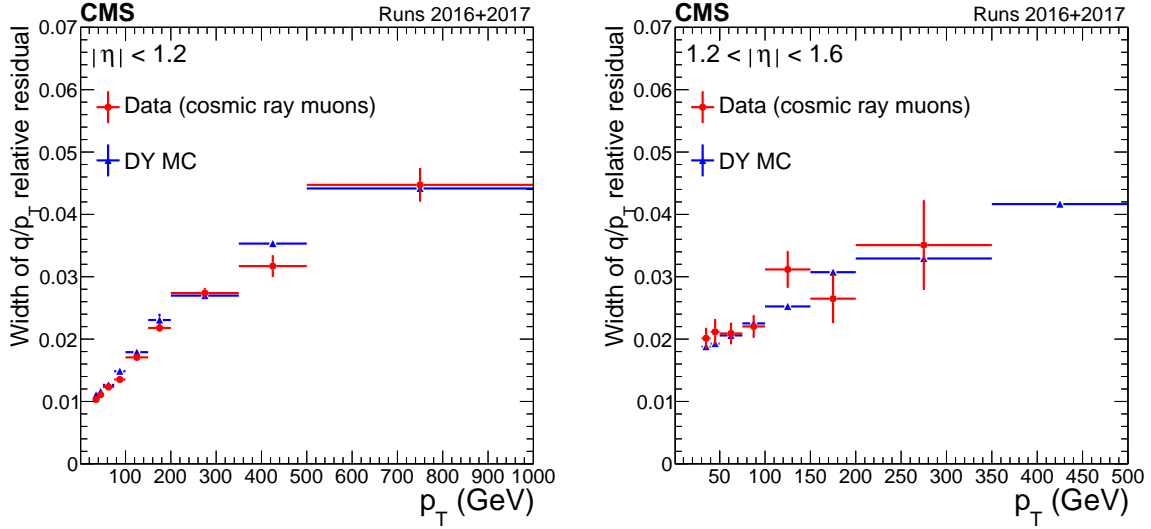


Figure 16. Gaussian σ of fits to q/p_T relative residuals for TuneP cosmic ray muons collected in 2016 and 2017 for (left) the barrel ($|\eta| < 1.2$) and (right) the endcap ($1.2 < |\eta| < 1.6$) regions, compared to the resolution extracted from DY simulation.

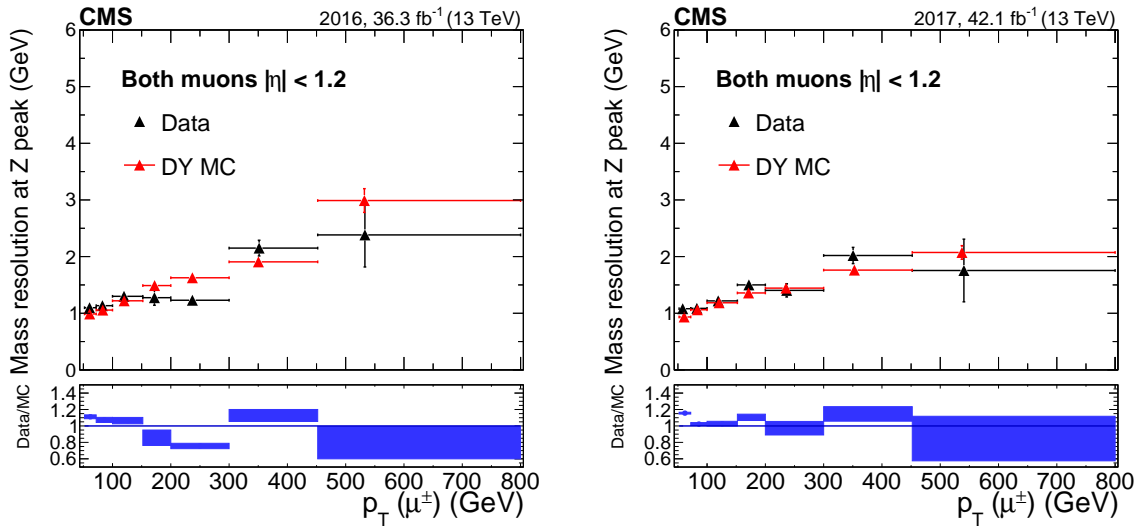


Figure 17. Dimuon mass resolution (Gaussian σ), as a function of muon TuneP p_T in the BB category. Each dimuon event is counted twice since each muon (μ^+ and μ^-) in the event is filling the histograms. Results for (left) 2016 and (right) 2017 are shown. Data are shown in black while the resolution obtained from simulation is shown in red. The lower panels of the plots show the ratio of data to simulation; the blue boxes represent the statistical uncertainties. The central value in each bin is obtained from the average of the distribution within the bin.

as a function of p_T is shown in figures 17 and 18 for events having both muons in the barrel (BB) or at least one of the two muons in the endcap (BE+EE), respectively. The BE+EE results are further split to isolate the forward endcap part (at least one of the two muons with $|\eta| > 1.6$) in the lower plot in figure 18.

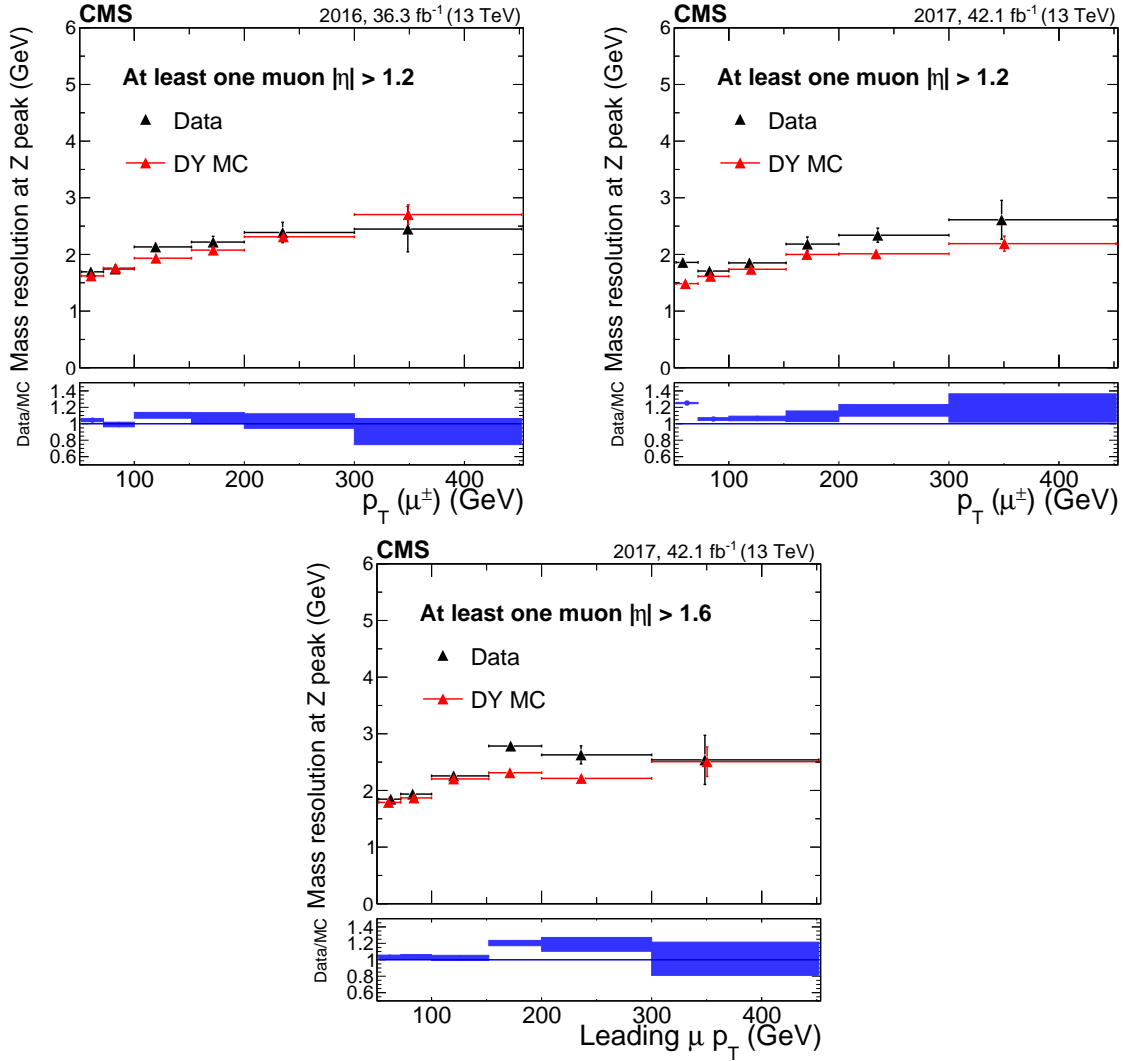


Figure 18. Dimuon mass resolution (Gaussian σ), as a function of muon TuneP p_T in the BE+EE category. Each dimuon event is counted twice since each muon (μ^+ and μ^-) in the event is filling the histograms. Results for (upper left) 2016 and (upper right) 2017 are shown. The lower plot is for 2017 data where the BE+EE category is defined with at least one of the two muons with $|\eta| > 1.6$. Data are shown in black while the resolution obtained from simulation is shown in red. The central value in each bin is obtained from the average of the distribution within the bin.

For the BB events, the mass resolution in data agrees with simulation for both 2016 and 2017 data. These results confirm what is observed with cosmic ray muons. Above 300 GeV the 2017 resolution is slightly better than that in 2016. This is due to changes in the muon system alignment and improved values of APEs. For the BE+EE events, an offset of about 15% can be seen over the entire p_T range in the 2017 data. The discrepancy is localized in the forward endcap region, as can be seen in the bottom plot of figure 18 that restricts the BE+EE category to events with only one of the two muons with $|\eta| > 1.6$. The results are presented as a function of the leading muon p_T ; the shift in the resolution between data and simulation is seen only when the events have at least one high- p_T muon. This endcap region is known to have a tracker alignment bias, as can also be seen in the scale results in figure 21.

6.3 Momentum scale from collision events

The scale of the muon p_T is sensitive to three effects that can potentially introduce biases: muon energy losses, detector misalignments, and magnetic field variations. The calibration of the momentum scale is performed by modifying the curvature of the muon, while taking into account these three physics effects. The detector alignment biases result in an additive correction k_b (to the (signed) muon curvature κ) that has the same sign for both positively and negatively charged muons, resulting in an increase in the measured p for one sign charge, and a decrease in measured p for the other sign. The variations from the magnetic field lead to a multiplicative correction factor to the curvature. The energy loss is taken into account with an additive term, that increases the muon momentum independent of the muon charge.

For intermediate- and low- p_T muons, two different methods are used for Run 2 data to estimate the additive and multiplicative correction factors to the muon curvature. The first method selects muons from Z boson decays and derives the corrections from the mean value of the distribution of q/p_T , with further tuning performed using the mean of the dimuon invariant mass spectrum [34]. The second method selects muons from Z boson, J/ψ , and $Y(1S)$ resonances, and determines corrections using a Kalman filter. The corrections are provided as a function of the muon η and ϕ in both methods and as a function of the muon p_T in the second method. In Run 2 data, the dominant source of scale bias is coming from the detector alignment.

For high- p_T muons, the reconstruction of the muon p_T relies both on the tracker and on the muon system inputs. Thus, the derived corrections from the two previous methods that focus only on the tracker information, are not directly applicable. In addition, the intrinsic alignment of the muon chambers within the muon system, and their alignment respectively to the tracker, are sources of potential scale bias. The generalized endpoint (GE) method [6] quantifies biases in the p_T determination relying on muons produced from DY events. The method consists of comparing the muon curvature distribution between data and simulated events, modifying the simulated values by a constant additive bias term (k_b), such that the distribution is distorted as $\kappa \rightarrow \kappa + k_b$. A χ^2 test is performed between the curvature distribution in data and in simulation, as a function of the injected bias k_b , in order to find the minimum of the distribution. Such a distortion reproduces a potential detector alignment bias that changes p in opposite directions for positively and negatively charged muons. The muon curvature without any additive bias in simulation is shown in figure 19.

The estimated additive biases measured with GE are presented as a function of η and ϕ , for the 2016 data in figure 20 and for the 2017 data in figure 21. For each year, the results are obtained using both the tracker and the TuneP p_T assignment. The sample size of high-momentum muons is limited, but it is visible that the detector parts that are most affected by the misalignment are the endcaps, in both years, with an estimated bias $k_b \approx 0.15/\text{TeV}$ in 2016 data and a maximum $k_b \approx 0.5/\text{TeV}$ in 2017 data localized in the forward positive endcap and in a given ϕ sector ($-60^\circ < \phi < 60^\circ$). No significant differences are found when comparing the bias values obtained with TuneP p_T and tracker p_T . Thus the misalignment is mostly coming from the tracker component while the muon system alignment does not contribute significantly. The local tracker misalignment found in 2017 data is suspected to be caused by radiation effects that impact the pixel and strip detector calibration throughout the run period. In addition, for that specific year the alignment procedure was limited by the sample size of muons from Z decays and from cosmic rays, which are needed to ensure the

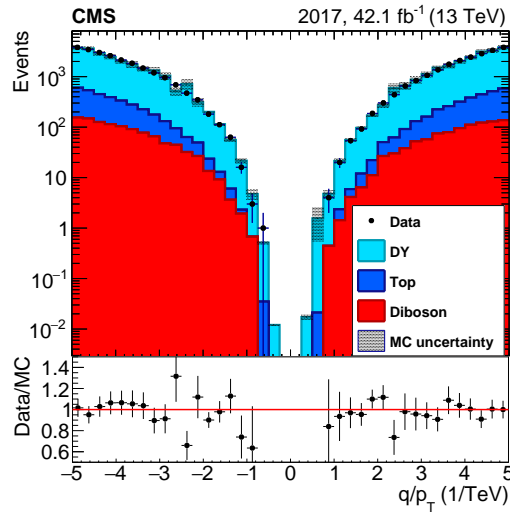


Figure 19. Data to simulation comparison of the curvature distribution in $Z \rightarrow \mu^+ \mu^-$ events, for 2017 data with muon $p_T > 200$ GeV.

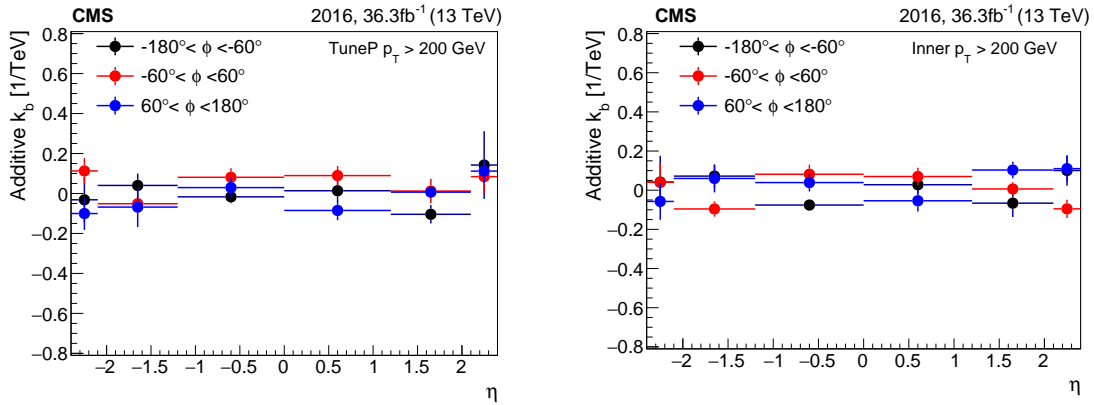


Figure 20. Measurement of the scale bias for muons above 200 GeV with 2016 data. On the left the p_T corresponds to TuneP, while on the right it corresponds to the tracker-only assignment.

right muon mixture input when performing the detector calibration. These results are in agreement with those from ref. [34].

7 Summary

The performance of muon reconstruction, identification, trigger, and momentum assignment has been studied in a sample enriched in high-momentum muons using proton-proton collisions at $\sqrt{s} = 13$ TeV, collected by the CMS experiment at the LHC in 2016–2017, and corresponding to the integrated luminosity of 78.4 fb^{-1} . Depending on the longitudinal component of the momentum, muons with transverse momentum $p_T > 200$ GeV can have radiative energy losses in steel that are no longer negligible compared to ionization energy losses. Dedicated methods have been developed

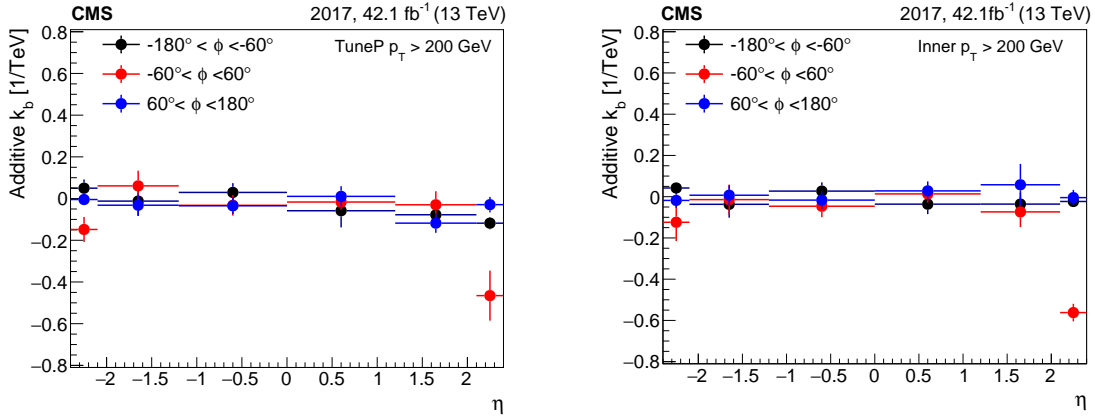


Figure 21. Measurement of the scale bias for muons above 200 GeV with 2017 data. On the left the p_T corresponds to the TuneP, while on the right it corresponds to the tracker-only assignment.

to study the performance impact of the detector alignment and electromagnetic showers along the muon track. Overall, the measurements are described accurately by the simulation and their reach in momentum is limited by the statistical uncertainties. The largest discrepancy between data and simulation is found at the trigger level with a 10% efficiency difference for muons with p_T around 1 TeV. Representative figures of merit that illustrate the muon performance at high momentum are listed below.

- The identification efficiency measured in data is $>98\%$ over the full p_T spectrum, up to 1000 GeV for a pseudorapidity magnitude $|\eta| < 2.4$. No dependence on the momentum p is observed. The ratio of data to simulation is within 1% of unity for $0 < |\eta| < 0.9$ and $2.1 < |\eta| < 2.4$, and within 0.5% for $0.9 < |\eta| < 2.1$.
- The standalone reconstruction efficiency measured in data is $>98\%$ over the full p_T spectrum and up to 1500 GeV for $|\eta| < 1.6$. No dependence on the momentum p is observed. The ratio of data to simulation is uniform and equal to 0.99. In the forward detector region ($|\eta| > 1.6$), an inefficiency trend starting at $p = 200$ GeV is observed both in simulation and in data, although it is slightly more pronounced in the latter. The muon showering and the dense track activities for muon momentum around 1000 GeV interfere within the muon reconstruction, and lead to a momentum dependence with up to 5% inefficiency when both effects are combined.
- The total trigger efficiency measured in data shows a decreasing trend from 92% at $p_T = 100$ GeV down to 80% at $p_T = 1000$ GeV, integrated over muon η . The simulation does not reproduce the severity of the slope and the ratio of data to simulation deviates from unity at the level of 10%. This discrepancy is driven by the first level (L1) trigger and is localized in the overlap region ($0.9 < |\eta| < 1.2$) because of a nonideal interplay between DT and CSC signals. This was improved in 2018.
- The L1 efficiency suffers from showering effects. Direct measurements from data and simulation are compared to a parameterization derived from showering inputs. The trend as a function of p is reproduced by the parameterization within the uncertainties. The biggest impact of showering is seen in the barrel region ($|\eta| < 0.9$), both in simulation and in data.

The simulation does not fully reproduce the slope seen in data in both barrel and endcap regions, thus indicating a slight underestimation of the showering effect at L1 in simulation.

- TuneP momentum assignment and performance is robust against the presence of showers. The simulation reproduces the choice of TuneP among the different TeV refitters in data.
- The Z boson mass resolution is <3 GeV for events with the leading muon p_T up to 450 GeV over the full η range. The Z boson mass resolution is very similar between simulation and data, except in the endcap region for the 2017 data, where a tracker alignment bias degrades the resolution by 20% for events with the leading muon p_T above 150 GeV.
- The trajectory curvature bias k_b is compatible with zero in the barrel region, but is as large as 0.5 TeV^{-1} for $|\eta| > 2.1$ in 2017 data.

These results show that the performance of the CMS detector is outstanding for high energy muons and is largely well described by simulation.

Acknowledgments

We congratulate our colleagues in the CERN accelerator departments for the excellent performance of the LHC and thank the technical and administrative staffs at CERN and at other CMS institutes for their contributions to the success of the CMS effort. In addition, we gratefully acknowledge the computing centers and personnel of the Worldwide LHC Computing Grid for delivering so effectively the computing infrastructure essential to our analyses. Finally, we acknowledge the enduring support for the construction and operation of the LHC and the CMS detector provided by the following funding agencies: the Austrian Federal Ministry of Education, Science and Research and the Austrian Science Fund; the Belgian Fonds de la Recherche Scientifique, and Fonds voor Wetenschappelijk Onderzoek; the Brazilian Funding Agencies (CNPq, CAPES, FAPERJ, FAPERGS, and FAPESP); the Bulgarian Ministry of Education and Science; CERN; the Chinese Academy of Sciences, Ministry of Science and Technology, and National Natural Science Foundation of China; the Colombian Funding Agency (COLCIENCIAS); the Croatian Ministry of Science, Education and Sport, and the Croatian Science Foundation; the Research Promotion Foundation, Cyprus; the Secretariat for Higher Education, Science, Technology and Innovation, Ecuador; the Ministry of Education and Research, Estonian Research Council via IUT23-4, IUT23-6 and PRG445 and European Regional Development Fund, Estonia; the Academy of Finland, Finnish Ministry of Education and Culture, and Helsinki Institute of Physics; the Institut National de Physique Nucléaire et de Physique des Particules/CNRS, and Commissariat à l'Énergie Atomique et aux Énergies Alternatives/CEA, France; the Bundesministerium für Bildung und Forschung, the Deutsche Forschungsgemeinschaft (DFG) under Germany's Excellence Strategy — EXC 2121 "Quantum Universe" — 390833306, and Helmholtz-Gemeinschaft Deutscher Forschungszentren, Germany; the General Secretariat for Research and Technology, Greece; the National Research, Development and Innovation Fund, Hungary; the Department of Atomic Energy and the Department of Science and Technology, India; the Institute for Studies in Theoretical Physics and Mathematics, Iran; the Science Foundation, Ireland; the Istituto Nazionale di Fisica Nucleare, Italy; the Ministry of Science, ICT and Future Planning, and National Research Foundation (NRF), Republic of Korea; the Ministry of Education and Science of the Republic of Latvia; the Lithuanian Academy of Sciences; the Ministry

of Education, and University of Malaya (Malaysia); the Ministry of Science of Montenegro; the Mexican Funding Agencies (BUAP, CINVESTAV, CONACYT, LNS, SEP, and UASLP-FAI); the Ministry of Business, Innovation and Employment, New Zealand; the Pakistan Atomic Energy Commission; the Ministry of Science and Higher Education and the National Science Centre, Poland; the Fundação para a Ciência e a Tecnologia, Portugal; JINR, Dubna; the Ministry of Education and Science of the Russian Federation, the Federal Agency of Atomic Energy of the Russian Federation, Russian Academy of Sciences, the Russian Foundation for Basic Research, and the National Research Center “Kurchatov Institute”; the Ministry of Education, Science and Technological Development of Serbia; the Secretaría de Estado de Investigación, Desarrollo e Innovación, Programa Consolider-Ingenio 2010, Plan Estatal de Investigación Científica y Técnica y de Innovación 2017–2020, research project IDI-2018-000174 del Principado de Asturias, and Fondo Europeo de Desarrollo Regional, Spain; the Ministry of Science, Technology and Research, Sri Lanka; the Swiss Funding Agencies (ETH Board, ETH Zurich, PSI, SNF, UniZH, Canton Zurich, and SER); the Ministry of Science and Technology, Taipei; the Thailand Center of Excellence in Physics, the Institute for the Promotion of Teaching Science and Technology of Thailand, Special Task Force for Activating Research and the National Science and Technology Development Agency of Thailand; the Scientific and Technical Research Council of Turkey, and Turkish Atomic Energy Authority; the National Academy of Sciences of Ukraine; the Science and Technology Facilities Council, U.K.; the U.S. Department of Energy, and the U.S. National Science Foundation.

Individuals have received support from the Marie-Curie program and the European Research Council and Horizon 2020 Grant, contract Nos. 675440, 752730, and 765710 (European Union); the Leventis Foundation; the A.P. Sloan Foundation; the Alexander von Humboldt Foundation; the Belgian Federal Science Policy Office; the Fonds pour la Formation à la Recherche dans l’Industrie et dans l’Agriculture (FRIA-Belgium); the Agentschap voor Innovatie door Wetenschap en Technologie (IWT-Belgium); the F.R.S.-FNRS and FWO (Belgium) under the “Excellence of Science — EOS” — be.h project n. 30820817; the Beijing Municipal Science & Technology Commission, No. Z181100004218003; the Ministry of Education, Youth and Sports (MEYS) of the Czech Republic; the Lendület (“Momentum”) Program and the János Bolyai Research Scholarship of the Hungarian Academy of Sciences, the New National Excellence Program ÚNKP, the NKFI research grants 123842, 123959, 124845, 124850, 125105, 128713, 128786, and 129058 (Hungary); the Council of Scientific and Industrial Research, India; the HOMING PLUS program of the Foundation for Polish Science, cofinanced from European Union, Regional Development Fund, the Mobility Plus program of the Ministry of Science and Higher Education, the National Science Center (Poland), contracts Harmonia 2014/14/M/ST2/00428, Opus 2014/13/B/ST2/02543, 2014/15/B/ST2/03998, and 2015/19/B/ST2/02861, Sonata-bis 2012/07/E/ST2/01406; the National Priorities Research Program by Qatar National Research Fund; the Ministry of Science and Education, grant no. 3.2989.2017 (Russia); the Programa de Excelencia María de Maeztu, and the Programa Severo Ochoa del Principado de Asturias; the Thalís and Aristeia programs cofinanced by EU-ESF, and the Greek NSRF; the Rachadapisek Sompot Fund for Postdoctoral Fellowship, Chulalongkorn University, and the Chulalongkorn Academic into Its 2nd Century Project Advancement Project (Thailand); the Nvidia Corporation; the Welch Foundation, contract C-1845; and the Weston Havens Foundation (U.S.A.).

References

- [1] A. Leike, *The Phenomenology of extra neutral gauge bosons*, *Phys. Rept.* **317** (1999) 143 [[hep-ph/9805494](#)].
- [2] P. Langacker, *The Physics of Heavy Z' Gauge Bosons*, *Rev. Mod. Phys.* **81** (2009) 1199 [[arXiv:0801.1345](#)].
- [3] K. Hsieh, K. Schmitz, J.-H. Yu and C.P. Yuan, *Global Analysis of General SU(2) × SU(2) × U(1) Models with Precision Data*, *Phys. Rev.* **D 82** (2010) 035011 [[arXiv:1003.3482](#)].
- [4] CMS collaboration, *The Performance of the CMS Muon Detector in Proton-Proton Collisions at $\sqrt{s} = 7$ TeV at the LHC*, *2013 JINST* **8** P11002 [[arXiv:1306.6905](#)].
- [5] CMS collaboration, *Performance of CMS Muon Reconstruction in pp Collision Events at $\sqrt{s} = 7$ TeV*, *2012 JINST* **7** P10002 [[arXiv:1206.4071](#)].
- [6] CMS collaboration, *Performance of the CMS muon detector and muon reconstruction with proton-proton collisions at $\sqrt{s} = 13$ TeV*, *2018 JINST* **13** P06015 [[arXiv:1804.04528](#)].
- [7] CMS collaboration, *The CMS trigger system*, *2017 JINST* **12** P01020 [[arXiv:1609.02366](#)].
- [8] CMS collaboration, *The CMS Experiment at the CERN LHC*, *2008 JINST* **3** S08004.
- [9] P. Nason, *A New method for combining NLO QCD with shower Monte Carlo algorithms*, *JHEP* **11** (2004) 040 [[hep-ph/0409146](#)].
- [10] S. Frixione, P. Nason and C. Oleari, *Matching NLO QCD computations with Parton Shower simulations: the POWHEG method*, *JHEP* **11** (2007) 070 [[arXiv:0709.2092](#)].
- [11] S. Alioli, P. Nason, C. Oleari and E. Re, *A general framework for implementing NLO calculations in shower Monte Carlo programs: the POWHEG BOX*, *JHEP* **06** (2010) 043 [[arXiv:1002.2581](#)].
- [12] J. Alwall et al., *The automated computation of tree-level and next-to-leading order differential cross sections and their matching to parton shower simulations*, *JHEP* **07** (2014) 079 [[arXiv:1405.0301](#)].
- [13] T. Sjöstrand et al., *An Introduction to PYTHIA 8.2*, *Comput. Phys. Commun.* **191** (2015) 159 [[arXiv:1410.3012](#)].
- [14] M. Czakon and A. Mitov, *Top++: A Program for the Calculation of the Top-Pair Cross-Section at Hadron Colliders*, *Comput. Phys. Commun.* **185** (2014) 2930 [[arXiv:1112.5675](#)].
- [15] CMS collaboration, *Underlying Event Tunes and Double Parton Scattering*, *CMS-PAS-GEN-14-001* (2014).
- [16] CMS collaboration, *Extraction and validation of a new set of CMS PYTHIA8 tunes from underlying-event measurements*, *CMS-PAS-GEN-17-001* (2018).
- [17] NNPDF collaboration, *Parton distributions for the LHC Run II*, *JHEP* **04** (2015) 040 [[arXiv:1410.8849](#)].
- [18] NNPDF collaboration, *Parton distributions from high-precision collider data*, *Eur. Phys. J.* **C 77** (2017) 663 [[arXiv:1706.00428](#)].
- [19] GEANT4 collaboration, *GEANT4: A Simulation toolkit*, *Nucl. Instrum. Meth.* **A 506** (2003) 250.
- [20] PARTICLE DATA GROUP collaboration, *Review of Particle Physics*, *Phys. Rev.* **D 98** (2018) 030001.
- [21] CMS collaboration, *Search for high-mass resonances in dilepton final states in proton-proton collisions at $\sqrt{s} = 13$ TeV*, *JHEP* **06** (2018) 120 [[arXiv:1803.06292](#)].

- [22] W. Adam, B. Mangano, T. Speer and T. Todorov, *Track Reconstruction in the CMS tracker*, [CMS-NOTE-2006-041](#) (2006).
- [23] R. Frühwirth, *Application of Kalman filtering to track and vertex fitting*, [Nucl. Instrum. Meth. A](#) **262** (1987) 444.
- [24] CMS collaboration, *Search for physics beyond the standard model in dilepton mass spectra in proton-proton collisions at $\sqrt{s} = 8$ TeV*, [JHEP](#) **04** (2015) 025 [[arXiv:1412.6302](#)].
- [25] CMS collaboration, *Description and performance of track and primary-vertex reconstruction with the CMS tracker*, [2014 JINST](#) **9** P10009 [[arXiv:1405.6569](#)].
- [26] CMS collaboration, *Alignment of the CMS Silicon Tracker during Commissioning with Cosmic Rays*, [2010 JINST](#) **5** T03009 [[arXiv:0910.2505](#)].
- [27] CMS collaboration, *Alignment of the CMS tracker with LHC and cosmic ray data*, [2014 JINST](#) **9** P06009 [[arXiv:1403.2286](#)].
- [28] CMS collaboration, *Performance of muon reconstruction including Alignment Position Errors for 2016 Collision Data*, [CMS-DP-2016-067](#) (2016).
- [29] CMS collaboration, *Alignment of the CMS Muon System with Cosmic-Ray and Beam-Halo Muons*, [2010 JINST](#) **5** T03020 [[arXiv:0911.4022](#)].
- [30] CMS collaboration, *Performance of CMS Muon Reconstruction in Cosmic-Ray Events*, [2010 JINST](#) **5** T03022 [[arXiv:0911.4994](#)].
- [31] LVD collaboration, *Measurement of cosmic muon charge ratio with the Large Volume Detector*, [arXiv:1311.6995](#).
- [32] M.J. Oreglia, *A study of the reactions $\psi' \rightarrow \gamma\gamma\psi$* , Ph.D. Thesis, Stanford University, Stanford California U.S.A. (1980).
- [33] J.E. Gaiser, *Charmonium spectroscopy from radiative decays of the J/ψ and ψ'* , Ph.D. Thesis, Stanford University, Stanford California U.S.A. (1982).
- [34] A. Bodek, A. van Dyne, J.Y. Han, W. Sakumoto and A. Strelnikov, *Extracting Muon Momentum Scale Corrections for Hadron Collider Experiments*, [Eur. Phys. J. C](#) **72** (2012) 2194 [[arXiv:1208.3710](#)].

The CMS collaboration

Yerevan Physics Institute, Yerevan, Armenia

A.M. Sirunyan[†], A. Tumasyan

Institut für Hochenergiephysik, Wien, Austria

W. Adam, F. Ambrogio, T. Bergauer, M. Dragicevic, J. Erö, A. Escalante Del Valle, M. Flechl, R. Frühwirth¹, M. Jeitler¹, N. Krammer, I. Krätschmer, D. Liko, T. Madlener, I. Mikulec, N. Rad, J. Schieck¹, R. Schöfbeck, M. Spanring, D. Spitzbart, W. Waltenberger, C.-E. Wulz¹, M. Zarucki

Institute for Nuclear Problems, Minsk, Belarus

V. Drugakov, V. Mossolov, J. Suarez Gonzalez

Universiteit Antwerpen, Antwerpen, Belgium

M.R. Darwish, E.A. De Wolf, D. Di Croce, X. Janssen, A. Lelek, M. Pieters, H. Rejeb Sfar, H. Van Havermaet, P. Van Mechelen, S. Van Putte, N. Van Remortel

Vrije Universiteit Brussel, Brussel, Belgium

F. Blekman, E.S. Bols, S.S. Chhibra, J. D'Hondt, J. De Clercq, D. Lontkovskyi, S. Lowette, I. Marchesini, S. Moortgat, Q. Python, K. Skovpen, S. Tavernier, W. Van Doninck, P. Van Mulders

Université Libre de Bruxelles, Bruxelles, Belgium

D. Beghin, B. Bilin, B. Clerbaux, G. De Lentdecker, H. Delannoy, B. Dorney, L. Favart, A. Grebenyuk, A.K. Kalsi, A. Popov, N. Postiau, E. Starling, L. Thomas, C. Vander Velde, P. Vanlaer, D. Vannerom

Ghent University, Ghent, Belgium

T. Cornelis, D. Dobur, I. Khvastunov², M. Niedziela, C. Roskas, M. Tytgat, W. Verbeke, B. Vermassen, M. Vit

Université Catholique de Louvain, Louvain-la-Neuve, Belgium

O. Bondu, G. Bruno, C. Caputo, P. David, C. Delaere, M. Delcourt, A. Giammanco, V. Lemaitre, J. Prisciandaro, A. Saggio, M. Vidal Marono, P. Vischia, S. Wuyckens, J. Zobec

Centro Brasileiro de Pesquisas Fisicas, Rio de Janeiro, Brazil

F.L. Alves, G.A. Alves, G. Correia Silva, C. Hensel, A. Moraes, P. Rebello Teles

Universidade do Estado do Rio de Janeiro, Rio de Janeiro, Brazil

E. Belchior Batista Das Chagas, W. Carvalho, J. Chinellato³, E. Coelho, E.M. Da Costa, G.G. Da Silveira⁴, D. De Jesus Damiao, C. De Oliveira Martins, S. Fonseca De Souza, L.M. Huertas Guativa, H. Malbouisson, J. Martins⁵, D. Matos Figueiredo, M. Medina Jaime⁶, M. Melo De Almeida, C. Mora Herrera, L. Mundim, H. Nogima, W.L. Prado Da Silva, L.J. Sanchez Rosas, A. Santoro, A. Sznajder, M. Thiel, E.J. Tonelli Manganote³, F. Torres Da Silva De Araujo, A. Vilela Pereira

Universidade Estadual Paulista^a, Universidade Federal do ABC^b, São Paulo, Brazil

C.A. Bernardes^a, L. Calligaris^a, T.R. Fernandez Perez Tomei^a, E.M. Gregores^b, D.S. Lemos, P.G. Mercadante^b, S.F. Novaes^a, SandraS. Padula^a

Institute for Nuclear Research and Nuclear Energy, Bulgarian Academy of Sciences, Sofia, Bulgaria

A. Aleksandrov, G. Antchev, R. Hadjiiska, P. Iaydjiev, M. Misheva, M. Rodozov, M. Shopova, G. Sultanov

University of Sofia, Sofia, Bulgaria

M. Bonchev, A. Dimitrov, T. Ivanov, L. Litov, B. Pavlov, P. Petkov

Beihang University, Beijing, China

W. Fang⁷, X. Gao⁷, L. Yuan

Institute of High Energy Physics, Beijing, China

G.M. Chen, H.S. Chen, M. Chen, C.H. Jiang, D. Leggat, H. Liao, Z. Liu, A. Spiezia, J. Tao, E. Yazgan, H. Zhang, S. Zhang⁸, J. Zhao

State Key Laboratory of Nuclear Physics and Technology, Peking University, Beijing, China

A. Agapitos, Y. Ban, G. Chen, A. Levin, J. Li, L. Li, Q. Li, Y. Mao, S.J. Qian, D. Wang, Q. Wang

Tsinghua University, Beijing, China

M. Ahmad, Z. Hu, Y. Wang

Zhejiang University, Hangzhou, China

M. Xiao

Universidad de Los Andes, Bogota, Colombia

C. Avila, A. Cabrera, C. Florez, C.F. González Hernández, M.A. Segura Delgado

Universidad de Antioquia, Medellin, Colombia

J. Mejia Guisao, J.D. Ruiz Alvarez, C.A. Salazar González, N. Vanegas Arbelaez

University of Split, Faculty of Electrical Engineering, Mechanical Engineering and Naval Architecture, Split, Croatia

D. Giljanović, N. Godinovic, D. Lelas, I. Puljak, T. Sculac

University of Split, Faculty of Science, Split, Croatia

Z. Antunovic, M. Kovac

Institute Rudjer Boskovic, Zagreb, Croatia

V. Brigljevic, D. Ferencek, K. Kadija, B. Mesic, M. Roguljic, A. Starodumov⁹, T. Susa

University of Cyprus, Nicosia, Cyprus

M.W. Ather, A. Attikis, E. Erodoutou, A. Ioannou, M. Kolosova, S. Konstantinou, G. Mavromanolakis, J. Mousa, C. Nicolaou, F. Ptochos, P.A. Razis, H. Rykaczewski, D. Tsiakkouri

Charles University, Prague, Czech Republic

M. Finger¹⁰, M. Finger Jr.¹⁰, A. Kveton, J. Tomsa

Escuela Politecnica Nacional, Quito, Ecuador

E. Ayala

Universidad San Francisco de Quito, Quito, Ecuador

E. Carrera Jarrin

Academy of Scientific Research and Technology of the Arab Republic of Egypt, Egyptian Network of High Energy Physics, Cairo, Egypt

H. Abdalla¹¹, S. Elgammal¹²

National Institute of Chemical Physics and Biophysics, Tallinn, Estonia

S. Bhowmik, A. Carvalho Antunes De Oliveira, R.K. Dewanjee, K. Ehataht, M. Kadastik, M. Raidal, C. Veelken

Department of Physics, University of Helsinki, Helsinki, Finland

P. Eerola, L. Forthomme, H. Kirschenmann, K. Osterberg, M. Voutilainen

Helsinki Institute of Physics, Helsinki, Finland

F. Garcia, J. Havukainen, J.K. Heikkilä, V. Karimäki, M.S. Kim, R. Kinnunen, T. Lampén, K. Lassila-Perini, S. Laurila, S. Lehti, T. Lindén, P. Luukka, T. Mäenpää, H. Siikonen, E. Tuominen, J. Tuominiemi

Lappeenranta University of Technology, Lappeenranta, Finland

T. Tuuva

IRFU, CEA, Université Paris-Saclay, Gif-sur-Yvette, France

M. Besancon, F. Couderc, M. Dejardin, D. Denegri, B. Fabbro, J.L. Faure, F. Ferri, S. Ganjour, A. Givernaud, P. Gras, G. Hamel de Monchenault, P. Jarry, C. Leloup, B. Lenzi, E. Locci, J. Malcles, J. Rander, A. Rosowsky, M.Ö. Sahin, A. Savoy-Navarro¹³, M. Titov, G.B. Yu

Laboratoire Leprince-Ringuet, CNRS/IN2P3, Ecole Polytechnique, Institut Polytechnique de Paris

S. Ahuja, C. Amendola, F. Beaudette, P. Busson, C. Charlot, B. Diab, G. Falmagne, R. Granier de Cassagnac, I. Kucher, A. Lobanov, C. Martin Perez, M. Nguyen, C. Ochando, P. Paganini, J. Rembser, R. Salerno, J.B. Sauvan, Y. Sirois, A. Zabi, A. Zghiche

Université de Strasbourg, CNRS, IPHC UMR 7178, Strasbourg, France

J.-L. Agram¹⁴, J. Andrea, D. Bloch, G. Bourgatte, J.-M. Brom, E.C. Chabert, C. Collard, E. Conte¹⁴, J.-C. Fontaine¹⁴, D. Gelé, U. Goerlach, M. Jansová, A.-C. Le Bihan, N. Tonon, P. Van Hove

Centre de Calcul de l'Institut National de Physique Nucleaire et de Physique des Particules, CNRS/IN2P3, Villeurbanne, France

S. Gadrat

Université de Lyon, Université Claude Bernard Lyon 1, CNRS-IN2P3, Institut de Physique Nucléaire de Lyon, Villeurbanne, France

S. Beauceron, C. Bernet, G. Boudoul, C. Camen, A. Carle, N. Chanon, R. Chierici, D. Contardo, P. Depasse, H. El Mamouni, J. Fay, S. Gascon, M. Gouzevitch, B. Ille, Sa. Jain, F. Lagarde, I.B. Laktineh, H. Lattaud, A. Lesauvage, M. Lethuillier, L. Mirabito, S. Perries, V. Sordini, L. Torterotot, G. Touquet, M. Vander Donckt, S. Viret

Georgian Technical University, Tbilisi, Georgia

T. Toriashvili¹⁵

Tbilisi State University, Tbilisi, Georgia

Z. Tsamalaidze¹⁰

RWTH Aachen University, I. Physikalisches Institut, Aachen, Germany

C. Autermann, L. Feld, K. Klein, M. Lipinski, D. Meuser, A. Pauls, M. Preuten, M.P. Rauch, J. Schulz, M. Teroerde, B. Wittmer

RWTH Aachen University, III. Physikalisches Institut A, Aachen, Germany

M. Erdmann, B. Fischer, S. Ghosh, T. Hebbeker, K. Hoepfner, H. Keller, L. Mastrolorenzo, M. Merschmeyer, A. Meyer, P. Millet, G. Mocellin, S. Mondal, S. Mukherjee, D. Noll, A. Novak, T. Pook, A. Pozdnyakov, T. Quast, M. Radziej, Y. Rath, H. Reithler, J. Roemer, A. Schmidt, S.C. Schuler, A. Sharma, S. Wiedenbeck, S. Zaleski

RWTH Aachen University, III. Physikalisches Institut B, Aachen, Germany

G. Flügge, W. Haj Ahmad¹⁶, O. Hlushchenko, T. Kress, T. Müller, A. Nowack, C. Pistone, O. Pooth, D. Roy, H. Sert, A. Stahl¹⁷

Deutsches Elektronen-Synchrotron, Hamburg, Germany

M. Aldaya Martin, P. Asmuss, I. Babounikau, H. Bakhshiansohi, K. Beernaert, O. Behnke, A. Bermúdez Martínez, D. Bertsche, A.A. Bin Anuar, K. Borras¹⁸, V. Botta, A. Campbell, A. Cardini, P. Connor, S. Consuegra Rodríguez, C. Contreras-Campana, V. Danilov, A. De Wit, M.M. Defranchis, C. Diez Pardos, D. Domínguez Damiani, G. Eckerlin, D. Eckstein, T. Eichhorn, A. Elwood, E. Eren, E. Gallo¹⁹, A. Geiser, A. Grohsjean, M. Guthoff, M. Haranko, A. Harb, A. Jafari, N.Z. Jomhari, H. Jung, A. Kasem¹⁸, M. Kasemann, H. Kaveh, J. Keaveney, C. Kleinwort, J. Knolle, D. Krücker, W. Lange, T. Lenz, J. Lidrych, K. Lipka, W. Lohmann²⁰, R. Mankel, I.-A. Melzer-Pellmann, A.B. Meyer, M. Meyer, M. Missiroli, J. Mnich, A. Mussgiller, V. Myronenko, D. Pérez Adán, S.K. Pflitsch, D. Pitzl, A. Raspereza, A. Saibel, M. Savitskyi, V. Scheurer, P. Schütze, C. Schwanenberger, R. Shevchenko, A. Singh, H. Tholen, O. Turkot, A. Vagnerini, M. Van De Klundert, R. Walsh, Y. Wen, K. Wichmann, C. Wissing, O. Zenaiev, R. Zlebcik

University of Hamburg, Hamburg, Germany

R. Aggleton, S. Bein, L. Benato, A. Benecke, V. Blobel, T. Dreyer, A. Ebrahimi, F. Feindt, A. Fröhlich, C. Garbers, E. Garutti, D. Gonzalez, P. Gunnellini, J. Haller, A. Hinzmann, A. Karavdina, G. Kasieczka, R. Klanner, R. Kogler, N. Kovalchuk, S. Kurz, V. Kutzner, J. Lange, T. Lange, A. Malara, J. Multhaupt, C.E.N. Niemeyer, A. Perieanu, A. Reimers, O. Rieger, C. Scharf, P. Schleper, S. Schumann, J. Schwandt, J. Sonneveld, H. Stadie, G. Steinbrück, F.M. Stober, B. Vormwald, I. Zoi

Karlsruher Institut fuer Technologie, Karlsruhe, Germany

M. Akbiyik, C. Barth, M. Baselga, S. Baur, T. Berger, E. Butz, R. Caspart, T. Chwalek, W. De Boer, A. Dierlamm, K. El Morabit, N. Faltermann, M. Giffels, P. Goldenzweig, A. Gottmann, M.A. Harrendorf, F. Hartmann¹⁷, U. Husemann, S. Kudella, S. Mitra, M.U. Mozer, D. Müller, Th. Müller, M. Musich, A. Nürnberg, G. Quast, K. Rabbertz, M. Schröder, I. Shvetsov, H.J. Simonis, R. Ulrich, M. Wassmer, M. Weber, C. Wöhrmann, R. Wolf

Institute of Nuclear and Particle Physics (INPP), NCSR Demokritos, Aghia Paraskevi, Greece

G. Anagnostou, P. Asenov, G. Daskalakis, T. Geralis, A. Kyriakis, D. Loukas, G. Paspalaki

National and Kapodistrian University of Athens, Athens, Greece

M. Diamantopoulou, G. Karathanasis, P. Kontaxakis, A. Manousakis-katsikakis, A. Panagiotou, I. Papavergou, N. Saoulidou, A. Stakia, K. Theofilatos, K. Vellidis, E. Vourliotis

National Technical University of Athens, Athens, Greece

G. Bakas, K. Kousouris, I. Papakrivopoulos, G. Tsipolitis

University of Ioánnina, Ioánnina, Greece

I. Evangelou, C. Foudas, P. Gianneios, P. Katsoulis, P. Kokkas, S. Mallios, K. Manitaras, N. Manthos, I. Papadopoulos, J. Stroligas, F.A. Triantis, D. Tsitsonis

MTA-ELTE Lendület CMS Particle and Nuclear Physics Group, Eötvös Loránd University, Budapest, Hungary

M. Bartók²¹, R. Chudasama, M. Csanad, P. Major, K. Mandal, A. Mehta, M.I. Nagy, G. Pasztor, O. Surányi, G.I. Veres

Wigner Research Centre for Physics, Budapest, Hungary

G. Bencze, C. Hajdu, D. Horvath²², F. Sikler, T.Á. Vámi, V. Veszpremi, G. Vesztergombi[†]

Institute of Nuclear Research ATOMKI, Debrecen, Hungary

N. Beni, S. Czellar, J. Karancsi²¹, J. Molnar, Z. Szillasi

Institute of Physics, University of Debrecen, Debrecen, Hungary

P. Raics, D. Teysier, Z.L. Trocsanyi, B. Ujvari

Eszterhazy Karoly University, Karoly Robert Campus, Gyongyos, Hungary

T. Csorgo, W.J. Metzger, F. Nemes, T. Novak

Indian Institute of Science (IISc), Bangalore, India

S. Choudhury, J.R. Komaragiri, P.C. Tiwari

National Institute of Science Education and Research, HBNI, Bhubaneswar, India

S. Bahinipati²⁴, C. Kar, G. Kole, P. Mal, V.K. Muraleedharan Nair Bindhu, A. Nayak²⁵, D.K. Sahoo²⁴, S.K. Swain

Panjab University, Chandigarh, India

S. Bansal, S.B. Beri, V. Bhatnagar, S. Chauhan, R. Chawla, N. Dhingra, R. Gupta, A. Kaur, M. Kaur, S. Kaur, P. Kumari, M. Lohan, M. Meena, K. Sandeep, S. Sharma, J.B. Singh, A.K. Viridi, G. Walia

University of Delhi, Delhi, India

A. Bhardwaj, B.C. Choudhary, R.B. Garg, M. Gola, S. Keshri, Ashok Kumar, M. Naimuddin, P. Priyanka, K. Ranjan, Aashaq Shah, R. Sharma

Saha Institute of Nuclear Physics, HBNI, Kolkata, India

R. Bhardwaj²⁶, M. Bharti²⁶, R. Bhattacharya, S. Bhattacharya, U. Bhawandeep²⁶, D. Bhowmik, S. Dutta, S. Ghosh, B. Gomber²⁷, M. Maity²⁸, K. Mondal, S. Nandan, A. Purohit, P.K. Rout, G. Saha, S. Sarkar, T. Sarkar²⁸, M. Sharan, B. Singh²⁶, S. Thakur²⁶

Indian Institute of Technology Madras, Madras, India

P.K. Behera, P. Kalbhor, A. Muhammad, P.R. Pujahari, A. Sharma, A.K. Sikdar

Bhabha Atomic Research Centre, Mumbai, India

D. Dutta, V. Jha, V. Kumar, D.K. Mishra, P.K. Netrakanti, L.M. Pant, P. Shukla

Tata Institute of Fundamental Research-A, Mumbai, India

T. Aziz, M.A. Bhat, S. Dugad, G.B. Mohanty, N. Sur, RavindraKumar Verma

Tata Institute of Fundamental Research-B, Mumbai, India

S. Banerjee, S. Bhattacharya, S. Chatterjee, P. Das, M. Guchait, S. Karmakar, S. Kumar, G. Majumder, K. Mazumdar, N. Sahoo, S. Sawant

Indian Institute of Science Education and Research (IISER), Pune, India

S. Dube, B. Kansal, A. Kapoor, K. Kothekar, S. Pandey, A. Rane, A. Rastogi, S. Sharma

Institute for Research in Fundamental Sciences (IPM), Tehran, Iran

S. Chenarani²⁹, E. Eskandari Tadavani, S.M. Etesami²⁹, M. Khakzad, M. Mohammadi Najafabadi, M. Naseri, F. Rezaei Hosseinabadi

University College Dublin, Dublin, Ireland

M. Felcini, M. Grunewald

INFN Sezione di Bari^a, Università di Bari^b, Politecnico di Bari^c, Bari, Italy

M. Abbrescia^{a,b}, R. Aly^{a,b,30}, C. Calabria^{a,b}, A. Colaleo^a, D. Creanza^{a,c}, L. Cristella^{a,b}, N. De Filippis^{a,c}, M. De Palma^{a,b}, A. Di Florio^{a,b}, W. Elmetenawee^{a,b}, L. Fiore^a, A. Gelmi^{a,b}, G. Iaselli^{a,c}, M. Ince^{a,b}, S. Lezki^{a,b}, G. Maggi^{a,c}, M. Maggi^a, J.A. Merlin, G. Miniello^{a,b}, S. My^{a,b}, S. Nuzzo^{a,b}, A. Pompili^{a,b}, G. Pugliese^{a,c}, R. Radogna^a, A. Ranieri^a, G. Selvaggi^{a,b}, L. Silvestris^a, F.M. Simone^{a,b}, R. Venditti^a, P. Verwilligen^a

INFN Sezione di Bologna^a, Università di Bologna^b, Bologna, Italy

G. Abbiendi^a, C. Battilana^{a,b}, D. Bonacorsi^{a,b}, L. Borgonovi^{a,b}, S. Braibant-Giacomelli^{a,b}, R. Campanini^{a,b}, P. Capiluppi^{a,b}, A. Castro^{a,b}, F.R. Cavallo^a, C. Ciocca^a, G. Codispoti^{a,b}, M. Cuffiani^{a,b}, G.M. Dallavalle^a, F. Fabbri^a, A. Fanfani^{a,b}, E. Fontanesi^{a,b}, P. Giacomelli^a, C. Grandi^a, L. Guiducci^{a,b}, F. Iemmi^{a,b}, S. Lo Meo^{a,31}, S. Marcellini^a, G. Masetti^a, F.L. Navarria^{a,b}, A. Perrotta^a, F. Primavera^{a,b}, A.M. Rossi^{a,b}, T. Rovelli^{a,b}, G.P. Siroli^{a,b}, N. Tosi^a

INFN Sezione di Catania^a, Università di Catania^b, Catania, Italy

S. Albergo^{a,b,32}, S. Costa^{a,b}, A. Di Mattia^a, R. Potenza^{a,b}, A. Tricomi^{a,b,32}, C. Tuve^{a,b}

INFN Sezione di Firenze^a, Università di Firenze^b, Firenze, Italy

G. Barbagli^a, A. Cassese, R. Ceccarelli, V. Ciulli^{a,b}, C. Civinini^a, R. D'Alessandro^{a,b}, F. Fiori^{a,c}, E. Focardi^{a,b}, G. Latino^{a,b}, P. Lenzi^{a,b}, M. Meschini^a, S. Paoletti^a, G. Sguazzoni^a, L. Viliani^a

INFN Laboratori Nazionali di Frascati, Frascati, Italy

L. Benussi, S. Bianco, D. Piccolo

INFN Sezione di Genova^a, Università di Genova^b, Genova, Italy

M. Bozzo^{a,b}, F. Ferro^a, R. Mulargia^{a,b}, E. Robutti^a, S. Tosi^{a,b}

INFN Sezione di Milano-Bicocca^a, Università di Milano-Bicocca^b, Milano, Italy

A. Benaglia^a, A. Beschi^{a,b}, F. Brivio^{a,b}, V. Ciriolo^{a,b,17}, M.E. Dinardo^{a,b}, P. Dini^a, S. Gennai^a, A. Ghezzi^{a,b}, P. Govoni^{a,b}, L. Guzzi^{a,b}, M. Malberti^a, S. Malvezzi^a, D. Menasce^a, F. Monti^{a,b}, L. Moroni^a, M. Paganoni^{a,b}, D. Pedrini^a, S. Ragazzi^{a,b}, T. Tabarelli de Fatis^{a,b}, D. Valsecchi^{a,b}, D. Zuolo^{a,b}

INFN Sezione di Napoli^a, Università di Napoli ‘Federico II’^b, Napoli, Italy, Università della Basilicata^c, Potenza, Italy, Università G. Marconi^d, Roma, Italy

S. Buontempo^a, N. Cavallo^{a,c}, A. De Iorio^{a,b}, A. Di Crescenzo^{a,b}, F. Fabozzi^{a,c}, F. Fienga^a, G. Galati^a, A.O.M. Iorio^{a,b}, L. Lista^{a,b}, S. Meola^{a,d,17}, P. Paolucci^{a,17}, B. Rossi^a, C. Sciacca^{a,b}, E. Voevodina^{a,b}

INFN Sezione di Padova^a, Università di Padova^b, Padova, Italy, Università di Trento^c, Trento, Italy

P. Azzi^a, N. Bacchetta^a, D. Bisello^{a,b}, A. Boletti^{a,b}, A. Bragagnolo^{a,b}, R. Carlin^{a,b}, P. Checchia^a, P. De Castro Manzano^a, T. Dorigo^a, U. Dosselli^a, F. Gasparini^{a,b}, U. Gasparini^{a,b}, A. Gozzelino^a, S.Y. Hoh^{a,b}, P. Lujan^a, M. Margoni^{a,b}, A.T. Meneguzzo^{a,b}, J. Pazzini^{a,b}, M. Presilla^b, P. Ronchese^{a,b}, R. Rossin^{a,b}, F. Simonetto^{a,b}, A. Tiko^a, M. Tosi^{a,b}, M. Zanetti^{a,b}, P. Zotto^{a,b}, G. Zumerle^{a,b}

INFN Sezione di Pavia^a, Università di Pavia^b, Pavia, Italy

A. Braghieri^a, D. Fiorina^{a,b}, P. Montagna^{a,b}, S.P. Ratti^{a,b}, V. Re^a, M. Ressegotti^{a,b}, C. Riccardi^{a,b}, P. Salvini^a, I. Vai^a, P. Vitulo^{a,b}

INFN Sezione di Perugia^a, Università di Perugia^b, Perugia, Italy

M. Biasini^{a,b}, G.M. Bilei^a, D. Ciangottini^{a,b}, L. Fanò^{a,b}, P. Lariccia^{a,b}, R. Leonardi^{a,b}, E. Manoni^a, G. Mantovani^{a,b}, V. Mariani^{a,b}, M. Menichelli^a, A. Rossi^{a,b}, A. Santocchia^{a,b}, D. Spiga^a

INFN Sezione di Pisa^a, Università di Pisa^b, Scuola Normale Superiore di Pisa^c, Pisa, Italy

K. Androsov^a, P. Azzurri^a, G. Bagliesi^a, V. Bertacchi^{a,c}, L. Bianchini^a, T. Boccali^a, R. Castaldi^a, M.A. Ciocci^{a,b}, R. Dell’Orso^a, S. Donato^a, G. Fedi^a, L. Giannini^{a,c}, A. Giassi^a, M.T. Grippo^a, F. Ligabue^{a,c}, E. Manca^{a,c}, G. Mandorli^{a,c}, A. Messineo^{a,b}, F. Palla^a, A. Rizzi^{a,b}, G. Rolandi³³, S. Roy Chowdhury, A. Scribano^a, P. Spagnolo^a, R. Tenchini^a, G. Tonelli^{a,b}, N. Turini, A. Venturi^a, P.G. Verdini^a

INFN Sezione di Roma^a, Sapienza Università di Roma^b, Rome, Italy

F. Cavallari^a, M. Cipriani^{a,b}, D. Del Re^{a,b}, E. Di Marco^a, M. Diemoz^a, E. Longo^{a,b}, P. Meridiani^a, G. Organtini^{a,b}, F. Pandolfi^a, R. Paramatti^{a,b}, C. Quaranta^{a,b}, S. Rahatlou^{a,b}, C. Rovelli^a, F. Santanastasio^{a,b}, L. Soffi^{a,b}

INFN Sezione di Torino^a, Università di Torino^b, Torino, Italy, Università del Piemonte Orientale^c, Novara, Italy

N. Amapane^{a,b}, R. Arcidiacono^{a,c}, S. Argiro^{a,b}, M. Arneodo^{a,c}, N. Bartosik^a, R. Bellan^{a,b}, A. Bellora, C. Biino^a, A. Cappati^{a,b}, N. Cartiglia^a, S. Cometti^a, M. Costa^{a,b}, R. Covarelli^{a,b}, N. Demaria^a, B. Kiani^{a,b}, F. Legger, C. Mariotti^a, S. Maselli^a, E. Migliore^{a,b}, V. Monaco^{a,b}, E. Monteil^{a,b}, M. Monteno^a, M.M. Obertino^{a,b}, G. Ortona^{a,b}, L. Pacher^{a,b}, N. Pastrone^a

M. Pelliccioni^a, G.L. Pinna Angioni^{a,b}, A. Romero^{a,b}, M. Ruspa^{a,c}, R. Salvatico^{a,b}, V. Sola^a,
A. Solano^{a,b}, D. Soldi^{a,b}, A. Staiano^a, D. Trocino^{a,b}

INFN Sezione di Trieste^a, Università di Trieste^b, Trieste, Italy

S. Belforte^a, V. Candelise^{a,b}, M. Casarsa^a, F. Cossutti^a, A. Da Rold^{a,b}, G. Della Ricca^{a,b},
F. Vazzoler^{a,b}, A. Zanetti^a

Kyungpook National University, Daegu, Korea

B. Kim, D.H. Kim, G.N. Kim, J. Lee, S.W. Lee, C.S. Moon, Y.D. Oh, S.I. Pak, S. Sekmen, D.C. Son,
Y.C. Yang

Chonnam National University, Institute for Universe and Elementary Particles, Kwangju, Korea

H. Kim, D.H. Moon, G. Oh

Hanyang University, Seoul, Korea

B. Francois, T.J. Kim, J. Park

Korea University, Seoul, Korea

S. Cho, S. Choi, Y. Go, S. Ha, B. Hong, K. Lee, K.S. Lee, J. Lim, J. Park, S.K. Park, Y. Roh, J. Yoo

Kyung Hee University, Department of Physics

J. Goh

Sejong University, Seoul, Korea

H.S. Kim

Seoul National University, Seoul, Korea

J. Almond, J.H. Bhyun, J. Choi, S. Jeon, J. Kim, J.S. Kim, H. Lee, K. Lee, S. Lee, K. Nam, M. Oh,
S.B. Oh, B.C. Radburn-Smith, U.K. Yang, H.D. Yoo, I. Yoon

University of Seoul, Seoul, Korea

D. Jeon, J.H. Kim, J.S.H. Lee, I.C. Park, I.J. Watson

Sungkyunkwan University, Suwon, Korea

Y. Choi, C. Hwang, Y. Jeong, J. Lee, Y. Lee, I. Yu

Riga Technical University, Riga, Latvia

V. Veckalns³⁴

Vilnius University, Vilnius, Lithuania

V. Dudenas, A. Juodagalvis, A. Rinkevicius, G. Tamulaitis, J. Vaitkus

National Centre for Particle Physics, Universiti Malaya, Kuala Lumpur, Malaysia

Z.A. Ibrahim, F. Mohamad Idris³⁵, W.A.T. Wan Abdullah, M.N. Yusli, Z. Zolkapli

Universidad de Sonora (UNISON), Hermosillo, Mexico

J.F. Benitez, A. Castaneda Hernandez, J.A. Murillo Quijada, L. Valencia Palomo

Centro de Investigacion y de Estudios Avanzados del IPN, Mexico City, Mexico

H. Castilla-Valdez, E. De La Cruz-Burelo, I. Heredia-De La Cruz³⁶, R. Lopez-Fernandez,
A. Sanchez-Hernandez

Universidad Iberoamericana, Mexico City, Mexico

S. Carrillo Moreno, C. Oropeza Barrera, M. Ramirez-Garcia, F. Vazquez Valencia

Benemerita Universidad Autonoma de Puebla, Puebla, Mexico

J. Eysermans, I. Pedraza, H.A. Salazar Ibarguen, C. Uribe Estrada

Universidad Autónoma de San Luis Potosí, San Luis Potosí, Mexico

A. Morelos Pineda

University of Montenegro, Podgorica, Montenegro

J. Mijuskovic², N. Raicevic

University of Auckland, Auckland, New Zealand

D. Krofcheck

University of Canterbury, Christchurch, New Zealand

S. Bheesette, P.H. Butler

National Centre for Physics, Quaid-I-Azam University, Islamabad, Pakistan

A. Ahmad, M. Ahmad, Q. Hassan, H.R. Hoorani, W.A. Khan, S. Qazi, M.A. Shah, M. Waqas

AGH University of Science and Technology Faculty of Computer Science, Electronics and Telecommunications, Krakow, Poland

V. Avati, L. Grzanka, M. Malawski

National Centre for Nuclear Research, Swierk, Poland

H. Bialkowska, M. Bluj, B. Boimska, M. Górski, M. Kazana, M. Szleper, P. Traczyk, P. Zalewski

Institute of Experimental Physics, Faculty of Physics, University of Warsaw, Warsaw, Poland

K. Bunkowski, A. Byszuk³⁷, K. Doroba, A. Kalinowski, M. Konecki, J. Krolikowski, M. Olszewski, M. Walczak

Laboratório de Instrumentação e Física Experimental de Partículas, Lisboa, Portugal

M. Araujo, P. Bargassa, D. Bastos, A. Di Francesco, P. Faccioli, B. Galinhas, M. Gallinaro, J. Hollar, N. Leonardo, T. Niknejad, J. Seixas, K. Shchelina, G. Strong, O. Toldaiev, J. Varela

Joint Institute for Nuclear Research, Dubna, Russia

S. Afanasiev, P. Bunin, M. Gavrilenko, I. Golutvin, I. Gorbunov, A. Kamenev, V. Karjavine, A. Lanev, A. Malakhov, V. Matveev^{38,39}, P. Moisenz, V. Palichik, V. Perelygin, M. Savina, S. Shmatov, S. Shulha, N. Skatchkov, V. Smirnov, N. Voytishin, A. Zarubin

Petersburg Nuclear Physics Institute, Gatchina (St. Petersburg), Russia

L. Chtchipounov, V. Golovtsov, Y. Ivanov, V. Kim⁴⁰, E. Kuznetsova⁴¹, P. Levchenko, V. Murzin, V. Oreshkin, I. Smirnov, D. Sosnov, V. Sulimov, L. Uvarov, A. Vorobyev

Institute for Nuclear Research, Moscow, Russia

Yu. Andreev, A. Dermenev, S. Gninenko, N. Golubev, A. Karneyeu, M. Kirsanov, N. Krasnikov, A. Pashenkov, D. Tlisov, A. Toropin

Institute for Theoretical and Experimental Physics named by A.I. Alikhanov of NRC ‘Kurchatov Institute’, Moscow, Russia

V. Epshteyn, V. Gavrilov, N. Lychkovskaya, A. Nikitenko⁴², V. Popov, I. Pozdnyakov, G. Safronov, A. Spiridonov, A. Stepennov, M. Toms, E. Vlasov, A. Zhokin

Moscow Institute of Physics and Technology, Moscow, Russia

T. Aushev

National Research Nuclear University ‘Moscow Engineering Physics Institute’ (MEPhI), Moscow, Russia

M. Chadeeva⁴³, P. Parygin, D. Philippov, E. Popova, V. Rusinov

P.N. Lebedev Physical Institute, Moscow, Russia

V. Andreev, M. Azarkin, I. Dremin, M. Kirakosyan, A. Terkulov

Skobeltsyn Institute of Nuclear Physics, Lomonosov Moscow State University, Moscow, Russia

A. Belyaev, E. Boos, M. Dubinin⁴⁴, L. Dudko, A. Ershov, A. Gribushin, A. Kaminskiy⁴⁵, V. Klyukhin, O. Kodolova, I. Lokhtin, S. Obraztsov, S. Petrushanko, V. Savrin

Novosibirsk State University (NSU), Novosibirsk, Russia

A. Barnyakov⁴⁶, V. Blinov⁴⁶, T. Dimova⁴⁶, L. Kardapoltsev⁴⁶, Y. Skovpen⁴⁶

Institute for High Energy Physics of National Research Centre ‘Kurchatov Institute’, Protvino, Russia

I. Azhgirey, I. Bayshev, S. Bitioukov, V. Kachanov, D. Konstantinov, P. Mandrik, V. Petrov, R. Ryutin, S. Slabospitskii, A. Sobol, S. Troshin, N. Tyurin, A. Uzunian, A. Volkov

National Research Tomsk Polytechnic University, Tomsk, Russia

A. Babaev, A. Iuzhakov, V. Okhotnikov

Tomsk State University, Tomsk, Russia

V. Borchsh, V. Ivanchenko, E. Tcherniaev

University of Belgrade: faculty of Physics and VINCA Institute of Nuclear Sciences

P. Adzic⁴⁷, P. Cirkovic, M. Dordevic, P. Milenovic, J. Milosevic, M. Stojanovic

Centro de Investigaciones Energéticas Medioambientales y Tecnológicas (CIEMAT), Madrid, Spain

M. Aguilar-Benitez, J. Alcaraz Maestre, A. Álvarez Fernández, I. Bachiller, M. Barrio Luna, CristinaF. Bedoya, J.A. Brochero Cifuentes, C.A. Carrillo Montoya, M. Cepeda, M. Cerrada, N. Colino, B. De La Cruz, A. Delgado Peris, J.P. Fernández Ramos, J. Flix, M.C. Fouz, O. Gonzalez Lopez, S. Goy Lopez, J.M. Hernandez, M.I. Josa, D. Moran, Á. Navarro Tobar, A. Pérez-Calero Yzquierdo, J. Puerta Pelayo, I. Redondo, L. Romero, S. Sánchez Navas, M.S. Soares, A. Triossi, C. Willmott

Universidad Autónoma de Madrid, Madrid, Spain

C. Albajar, J.F. de Trocóniz, R. Reyes-Almanza

Universidad de Oviedo, Instituto Universitario de Ciencias y Tecnologías Espaciales de Asturias (ICTEA), Oviedo, Spain

B. Alvarez Gonzalez, J. Cuevas, C. Erice, J. Fernandez Menendez, S. Folgueras, I. Gonzalez Caballero, J.R. González Fernández, E. Palencia Cortezon, V. Rodríguez Bouza, S. Sanchez Cruz

Instituto de Física de Cantabria (IFCA), CSIC-Universidad de Cantabria, Santander, Spain

I.J. Cabrillo, A. Calderon, B. Chazin Quero, J. Duarte Campderros, M. Fernandez, P.J. Fernández Manteca, A. García Alonso, G. Gomez, C. Martinez Rivero, P. Martinez Ruiz del Arbol, F. Matorras, J. Piedra Gomez, C. Prieels, T. Rodrigo, A. Ruiz-Jimeno, L. Russo⁴⁸, L. Scodellaro, I. Vila, J.M. Vizán García

University of Colombo, Colombo, Sri Lanka

K. Malagalage

University of Ruhuna, Department of Physics, Matara, Sri Lanka

W.G.D. Dharmaratna, N. Wickramage

CERN, European Organization for Nuclear Research, Geneva, Switzerland

D. Abbaneo, B. Akgun, E. Auffray, G. Auzinger, J. Baechler, P. Baillon, A.H. Ball, D. Barney, J. Bendavid, M. Bianco, A. Bocci, P. Bortignon, E. Bossini, E. Brondolin, T. Camporesi, A. Caratelli, G. Cerminara, E. Chapon, G. Cucciati, D. d’Enterria, A. Dabrowski, N. Daci, V. Daponte, A. David, O. Davignon, A. De Roeck, M. Deile, M. Dobson, M. Dünser, N. Dupont, A. Elliott-Peisert, N. Emriskova, F. Fallavollita⁴⁹, D. Fasanella, S. Fiorendi, G. Franzoni, J. Fulcher, W. Funk, S. Giani, D. Gigi, K. Gill, F. Glege, L. Gouskos, M. Gruchala, M. Guilbaud, D. Gulhan, J. Hegeman, C. Heidegger, Y. Iiyama, V. Innocente, T. James, P. Janot, O. Karacheban²⁰, J. Kaspar, J. Kieseler, M. Krammer¹, N. Kratochwil, C. Lange, P. Lecoq, C. Lourenço, L. Malgeri, M. Mannelli, A. Massironi, F. Meijers, S. Mersi, E. Meschi, F. Moortgat, M. Mulders, J. Ngadiuba, J. Niedziela, S. Nourbakhsh, S. Orfanelli, L. Orsini, F. Pantaleo¹⁷, L. Pape, E. Perez, M. Peruzzi, A. Petrilli, G. Petrucciani, A. Pfeiffer, M. Pierini, F.M. Pitters, D. Rabady, A. Racz, M. Rieger, M. Rovere, H. Sakulin, J. Salfeld-Nebgen, C. Schäfer, C. Schwick, M. Selvaggi, A. Sharma, P. Silva, W. Snoeys, P. Sphicas⁵⁰, J. Steggemann, S. Summers, V.R. Tavolaro, D. Treille, A. Tsiros, G.P. Van Onsem, A. Vartak, M. Verzetti, W.D. Zeuner

Paul Scherrer Institut, Villigen, Switzerland

L. Caminada⁵¹, K. Deiters, W. Erdmann, R. Horisberger, Q. Ingram, H.C. Kaestli, D. Kotlinski, U. Langenegger, T. Rohe, S.A. Wiederkehr

ETH Zurich — Institute for Particle Physics and Astrophysics (IPA), Zurich, Switzerland

M. Backhaus, P. Berger, N. Chernyavskaya, G. Dissertori, M. Dittmar, M. Donegà, C. Dorfer, T.A. Gómez Espinosa, C. Grab, D. Hits, W. Lustermann, R.A. Manzoni, M.T. Meinhard, F. Micheli, P. Musella, F. Nessi-Tedaldi, F. Pauss, G. Perrin, L. Perrozzi, S. Pigazzini, M.G. Ratti, M. Reichmann, C. Reissel, T. Reitenspiess, B. Ristic, D. Ruini, D.A. Sanz Becerra, M. Schönenberger, L. Shchutska, M.L. Vesterbacka Olsson, R. Wallny, D.H. Zhu

Universität Zürich, Zurich, Switzerland

T.K. Aarrestad, C. AMSLER⁵², C. Botta, D. Brzdechko, M.F. Canelli, A. De Cosa, R. Del Burgo, B. Kilminster, S. Leontsinis, V.M. Mikuni, I. Neutelings, G. Rauco, P. Robmann, K. Schweiger, C. Seitz, Y. Takahashi, S. Wertz, A. Zucchetta

National Central University, Chung-Li, Taiwan

T.H. Doan, C.M. Kuo, W. Lin, A. Roy, S.S. Yu

National Taiwan University (NTU), Taipei, Taiwan

P. Chang, Y. Chao, K.F. Chen, P.H. Chen, W.-S. Hou, Y.y. Li, R.-S. Lu, E. Paganis, A. Psallidas, A. Steen

Chulalongkorn University, Faculty of Science, Department of Physics, Bangkok, Thailand

B. Asavapibhop, C. Asawatangtrakuldee, N. Srimanobhas, N. Suwonjandee

Çukurova University, Physics Department, Science and Art Faculty, Adana, Turkey

A. Bat, F. Boran, A. Celik⁵³, S. Damarseckin⁵⁴, Z.S. Demiroglu, F. Dolek, C. Dozen⁵⁵, I. Dumanoglu, G. Gokbulut, EmineGurpinar Guler⁵⁶, Y. Guler, I. Hos⁵⁷, C. Isik, E.E. Kangal⁵⁸, O. Kara, A. Kayis Topaksu, U. Kiminsu, G. Onengut, K. Ozdemir⁵⁹, S. Ozturk⁶⁰, A.E. Simsek, U.G. Tok, S. Turkcapar, I.S. Zorbakir, C. Zorbilmez

Middle East Technical University, Physics Department, Ankara, Turkey

B. Isildak⁶¹, G. Karapinar⁶², M. Yalvac

Bogazici University, Istanbul, Turkey

I.O. Atakisi, E. Gülmez, M. Kaya⁶³, O. Kaya⁶⁴, Ö. Özçelik, S. Tekten, E.A. Yetkin⁶⁵

Istanbul Technical University, Istanbul, Turkey

A. Cakir, K. Cankocak, Y. Komurcu, S. Sen⁶⁶

Istanbul University, Istanbul, Turkey

S. Cerci⁶⁷, B. Kaynak, S. Ozkorucuklu, D. Sunar Cerci⁶⁷

Institute for Scintillation Materials of National Academy of Science of Ukraine, Kharkov, Ukraine

B. Grynyov

National Scientific Center, Kharkov Institute of Physics and Technology, Kharkov, Ukraine

L. Levchuk

University of Bristol, Bristol, United Kingdom

E. Bhal, S. Bologna, J.J. Brooke, D. Burns⁶⁸, E. Clement, D. Cussans, H. Flacher, J. Goldstein, G.P. Heath, H.F. Heath, L. Kreczko, B. Krikler, S. Paramesvaran, B. Penning, T. Sakuma, S. Seif El Nasr-Storey, V.J. Smith, J. Taylor, A. Titterton

Rutherford Appleton Laboratory, Didcot, United Kingdom

K.W. Bell, A. Belyaev⁶⁹, C. Brew, R.M. Brown, D.J.A. Cockerill, J.A. Coughlan, K. Harder, S. Harper, J. Linacre, K. Manolopoulos, D.M. Newbold, E. Olaiya, D. Petyt, T. Reis, T. Schuh, C.H. Shepherd-Themistocleous, A. Thea, I.R. Tomalin, T. Williams

Imperial College, London, United Kingdom

R. Bainbridge, P. Bloch, J. Borg, S. Breeze, O. Buchmuller, A. Bundock, GurpreetSingh CHAHAL⁷⁰, D. Colling, P. Dauncey, G. Davies, M. Della Negra, R. Di Maria, P. Everaerts, G. Hall, G. Iles, M. Komm, L. Lyons, A.-M. Magnan, S. Malik, A. Martelli, V. Milosevic,

A. Morton, J. Nash⁷¹, V. Palladino, M. Pesaresi, D.M. Raymond, A. Richards, A. Rose, E. Scott, C. Seez, A. Shtipliyski, M. Stoye, T. Strebler, A. Tapper, K. Uchida, T. Virdee¹⁷, N. Wardle, D. Winterbottom, A.G. Zecchinelli, S.C. Zenz

Brunel University, Uxbridge, United Kingdom

J.E. Cole, P.R. Hobson, A. Khan, P. Kyberd, C.K. Mackay, I.D. Reid, L. Teodorescu, S. Zahid

Baylor University, Waco, U.S.A.

K. Call, B. Caraway, J. Dittmann, K. Hatakeyama, C. Madrid, B. McMaster, N. Pastika, C. Smith

Catholic University of America, Washington, DC, U.S.A.

R. Bartek, A. Dominguez, R. Uniyal, A.M. Vargas Hernandez

The University of Alabama, Tuscaloosa, U.S.A.

A. Buccilli, S.I. Cooper, C. Henderson, P. Rumerio, C. West

Boston University, Boston, U.S.A.

A. Albert, D. Arcaro, Z. Demiragli, D. Gastler, C. Richardson, J. Rohlf, D. Sperka, I. Suarez, L. Sulak, D. Zou

Brown University, Providence, U.S.A.

G. Benelli, B. Burkley, X. Coubez¹⁸, D. Cutts, Y.t. Duh, M. Hadley, U. Heintz, J.M. Hogan⁷², K.H.M. Kwok, E. Laird, G. Landsberg, K.T. Lau, J. Lee, M. Narain, S. Sagir⁷³, R. Syarif, E. Usai, W.Y. Wong, D. Yu, W. Zhang

University of California, Davis, Davis, U.S.A.

R. Band, C. Brainerd, R. Breedon, M. Calderon De La Barca Sanchez, M. Chertok, J. Conway, R. Conway, P.T. Cox, R. Erbacher, C. Flores, G. Funk, F. Jensen, W. Ko[†], O. Kukral, R. Lander, M. Mulhearn, D. Pellett, J. Pilot, M. Shi, D. Taylor, K. Tos, M. Tripathi, Z. Wang, F. Zhang

University of California, Los Angeles, U.S.A.

M. Bachtis, C. Bravo, R. Cousins, A. Dasgupta, A. Florent, J. Hauser, M. Ignatenko, N. Mccoll, W.A. Nash, S. Regnard, D. Saltzberg, C. Schnaible, B. Stone, V. Valuev

University of California, Riverside, Riverside, U.S.A.

K. Burt, Y. Chen, R. Clare, J.W. Gary, S.M.A. Ghiasi Shirazi, G. Hanson, G. Karapostoli, O.R. Long, M. Olmedo Negrete, M.I. Paneva, W. Si, L. Wang, S. Wimpenny, B.R. Yates, Y. Zhang

University of California, San Diego, La Jolla, U.S.A.

J.G. Branson, P. Chang, S. Cittolin, S. Cooperstein, N. Deelen, M. Derdzinski, R. Gerosa, D. Gilbert, B. Hashemi, D. Klein, V. Krutelyov, J. Letts, M. Masciovecchio, S. May, S. Padhi, M. Pieri, V. Sharma, M. Tadel, F. Würthwein, A. Yagil, G. Zevi Della Porta

University of California, Santa Barbara — Department of Physics, Santa Barbara, U.S.A.

N. Amin, R. Bhandari, C. Campagnari, M. Citron, V. Dutta, M. Franco Sevilla, J. Incandela, B. Marsh, H. Mei, A. Ovcharova, H. Qu, J. Richman, U. Sarica, D. Stuart, S. Wang

California Institute of Technology, Pasadena, U.S.A.

D. Anderson, A. Bornheim, O. Cerri, I. Dutta, J.M. Lawhorn, N. Lu, J. Mao, H.B. Newman, T.Q. Nguyen, J. Pata, M. Spiropulu, J.R. Vlimant, S. Xie, Z. Zhang, R.Y. Zhu

Carnegie Mellon University, Pittsburgh, U.S.A.

M.B. Andrews, T. Ferguson, T. Mudholkar, M. Paulini, M. Sun, I. Vorobiev, M. Weinberg

University of Colorado Boulder, Boulder, U.S.A.

J.P. Cumalat, W.T. Ford, E. MacDonald, T. Mulholland, R. Patel, A. Perloff, K. Stenson, K.A. Ulmer, S.R. Wagner

Cornell University, Ithaca, U.S.A.

J. Alexander, Y. Cheng, J. Chu, A. Datta, A. Frankenthal, K. Mcdermott, J.R. Patterson, D. Quach, A. Ryd, S.M. Tan, Z. Tao, J. Thom, P. Wittich, M. Zientek

Fermi National Accelerator Laboratory, Batavia, U.S.A.

S. Abdullin, M. Albrow, M. Alyari, G. Apollinari, A. Apresyan, A. Apyan, S. Banerjee, L.A.T. Bauerdick, A. Beretvas, D. Berry, J. Berryhill, P.C. Bhat, K. Burkett, J.N. Butler, A. Canepa, G.B. Cerati, H.W.K. Cheung, F. Chlebana, M. Cremonesi, J. Duarte, V.D. Elvira, J. Freeman, Z. Gecse, E. Gottschalk, L. Gray, D. Green, S. Grünendahl, O. Gutsche, J. Hanlon, R.M. Harris, S. Hasegawa, R. Heller, J. Hirschauer, B. Jayatilaka, S. Jindariani, M. Johnson, U. Joshi, T. Klijnsma, B. Klima, M.J. Kortelainen, B. Kreis, S. Lammel, J. Lewis, D. Lincoln, R. Lipton, M. Liu, T. Liu, J. Lykken, K. Maeshima, J.M. Marraffino, D. Mason, P. McBride, P. Merkel, S. Mrenna, S. Nahn, V. O'Dell, V. Papadimitriou, K. Pedro, C. Pena, G. Rakness, F. Ravera, A. Reinsvold Hall, L. Ristori, B. Schneider, E. Sexton-Kennedy, N. Smith, A. Soha, W.J. Spalding, L. Spiegel, S. Stoynev, J. Strait, N. Strobbe, L. Taylor, S. Tkaczyk, N.V. Tran, L. Uplegger, E.W. Vaandering, C. Vernieri, R. Vidal, M. Wang, H.A. Weber

University of Florida, Gainesville, U.S.A.

D. Acosta, P. Avery, D. Bourilkov, A. Brinkerhoff, L. Cadamuro, V. Cherepanov, F. Errico, R.D. Field, S.V. Gleyzer, D. Guerrero, B.M. Joshi, M. Kim, J. Konigsberg, A. Korytov, K.H. Lo, K. Matchev, N. Menendez, G. Mitselmakher, D. Rosenzweig, K. Shi, J. Wang, S. Wang, X. Zuo

Florida International University, Miami, U.S.A.

Y.R. Joshi

Florida State University, Tallahassee, U.S.A.

T. Adams, A. Askew, S. Hagopian, V. Hagopian, K.F. Johnson, R. Khurana, T. Kolberg, G. Martinez, T. Perry, H. Prosper, C. Schiber, R. Yohay, J. Zhang

Florida Institute of Technology, Melbourne, U.S.A.

M.M. Baarmand, M. Hohlmann, D. Noonan, M. Rahmani, M. Saunders, F. Yumiceva

University of Illinois at Chicago (UIC), Chicago, U.S.A.

M.R. Adams, L. Apanasevich, R.R. Betts, R. Cavanaugh, X. Chen, S. Dittmer, O. Evdokimov, C.E. Gerber, D.A. Hangal, D.J. Hofman, C. Mills, T. Roy, M.B. Tonjes, N. Varelas, J. Viinikainen, H. Wang, X. Wang, Z. Wu

The University of Iowa, Iowa City, U.S.A.

M. Alhusseini, B. Bilki⁵⁶, K. Dilsiz⁷⁴, S. Durgut, R.P. Gandrajula, M. Haytmyradov, V. Khristenko, O.K. Köseyan, J.-P. Merlo, A. Mestvirishvili⁷⁵, A. Moeller, J. Nachtman, H. Ogul⁷⁶, Y. Onel, F. Ozok⁷⁷, A. Penzo, C. Snyder, E. Tiras, J. Wetzel

Johns Hopkins University, Baltimore, U.S.A.

B. Blumenfeld, A. Cocoros, N. Eminizer, A.V. Gritsan, W.T. Hung, S. Kyriacou, P. Maksimovic, J. Roskes, M. Swartz

The University of Kansas, Lawrence, U.S.A.

C. Baldenegro Barrera, P. Baringer, A. Bean, S. Boren, J. Bowen, A. Bylinkin, T. Isidori, S. Khalil, J. King, G. Krintiras, A. Kropivnitskaya, C. Lindsey, D. Majumder, W. Mcbrayer, N. Minafra, M. Murray, C. Rogan, C. Royon, S. Sanders, E. Schmitz, J.D. Tapia Takaki, Q. Wang, J. Williams, G. Wilson

Kansas State University, Manhattan, U.S.A.

S. Duric, A. Ivanov, K. Kaadze, D. Kim, Y. Maravin, D.R. Mendis, T. Mitchell, A. Modak, A. Mohammadi

Lawrence Livermore National Laboratory, Livermore, U.S.A.

F. Rebassoo, D. Wright

University of Maryland, College Park, U.S.A.

A. Baden, O. Baron, A. Belloni, S.C. Eno, Y. Feng, N.J. Hadley, S. Jabeen, G.Y. Jeng, R.G. Kellogg, A.C. Mignerey, S. Nabili, F. Ricci-Tam, M. Seidel, Y.H. Shin, A. Skuja, S.C. Tonwar, K. Wong

Massachusetts Institute of Technology, Cambridge, U.S.A.

D. Abercrombie, B. Allen, A. Baty, R. Bi, S. Brandt, W. Busza, I.A. Cali, M. D'Alfonso, G. Gomez Ceballos, M. Goncharov, P. Harris, D. Hsu, M. Hu, M. Klute, D. Kovalskyi, Y.-J. Lee, P.D. Luckey, B. Maier, A.C. Marini, C. McGinn, C. Mironov, S. Narayanan, X. Niu, C. Paus, D. Rankin, C. Roland, G. Roland, Z. Shi, G.S.F. Stephans, K. Sumorok, K. Tatar, D. Velicanu, J. Wang, T.W. Wang, B. Wyslouch

University of Minnesota, Minneapolis, U.S.A.

R.M. Chatterjee, A. Evans, S. Guts[†], P. Hansen, J. Hiltbrand, Sh. Jain, Y. Kubota, Z. Lesko, J. Mans, M. Revering, R. Rusack, R. Saradhy, N. Schroeder, M.A. Wadud

University of Mississippi, Oxford, U.S.A.

J.G. Acosta, S. Oliveros

University of Nebraska-Lincoln, Lincoln, U.S.A.

K. Bloom, S. Chauhan, D.R. Claes, C. Fangmeier, L. Finco, F. Golf, R. Kamalieddin, I. Kravchenko, J.E. Siado, G.R. Snow[†], B. Stieger, W. Tabb

State University of New York at Buffalo, Buffalo, U.S.A.

G. Agarwal, C. Harrington, I. Iashvili, A. Kharchilava, C. McLean, D. Nguyen, A. Parker, J. Pekkanen, S. Rappoccio, B. Roozbahani

Northeastern University, Boston, U.S.A.

G. Alverson, E. Barberis, C. Freer, Y. Haddad, A. Hortiangtham, G. Madigan, B. Marzocchi, D.M. Morse, T. Orimoto, L. Skinnari, A. Tishelman-Charny, T. Wamorkar, B. Wang, A. Wisecarver, D. Wood

Northwestern University, Evanston, U.S.A.

S. Bhattacharya, J. Bueghly, A. Gilbert, T. Gunter, K.A. Hahn, N. Odell, M.H. Schmitt, K. Sung, M. Trovato, M. Velasco

University of Notre Dame, Notre Dame, U.S.A.

R. Bucci, N. Dev, R. Goldouzian, M. Hildreth, K. Hurtado Anampa, C. Jessop, D.J. Karmgard, K. Lannon, W. Li, N. Loukas, N. Marinelli, I. Mcalister, F. Meng, Y. Musienko³⁸, R. Ruchti, P. Siddireddy, G. Smith, S. Taroni, M. Wayne, A. Wightman, M. Wolf, A. Woodard

The Ohio State University, Columbus, U.S.A.

J. Alimena, B. Bylsma, L.S. Durkin, B. Francis, C. Hill, W. Ji, A. Lefeld, T.Y. Ling, B.L. Winer

Princeton University, Princeton, U.S.A.

G. Dezoort, P. Elmer, J. Hardenbrook, N. Haubrich, S. Higginbotham, A. Kalogeropoulos, S. Kwan, D. Lange, M.T. Lucchini, J. Luo, D. Marlow, K. Mei, I. Ojalvo, J. Olsen, C. Palmer, P. Piroué, D. Stickland, C. Tully

University of Puerto Rico, Mayaguez, U.S.A.

S. Malik, S. Norberg

Purdue University, West Lafayette, U.S.A.

A. Barker, V.E. Barnes, S. Das, L. Gutay, M. Jones, A.W. Jung, A. Khatiwada, B. Mahakud, D.H. Miller, G. Negro, N. Neumeister, C.C. Peng, S. Piperov, H. Qiu, J.F. Schulte, N. Trevisani, F. Wang, R. Xiao, W. Xie

Purdue University Northwest, Hammond, U.S.A.

T. Cheng, J. Dolen, N. Parashar

Rice University, Houston, U.S.A.

U. Behrens, S. Dildick, K.M. Ecklund, S. Freed, F.J.M. Geurts, M. Kilpatrick, Arun Kumar, W. Li, B.P. Padley, R. Redjimi, J. Roberts, J. Rorie, W. Shi, A.G. Stahl Leiton, Z. Tu, A. Zhang

University of Rochester, Rochester, U.S.A.

A. Bodek, P. de Barbaro, R. Demina, J.L. Dulemba, C. Fallon, T. Ferbel, M. Galanti, A. Garcia-Bellido, O. Hindrichs, A. Khukhunaishvili, E. Ranken, R. Taus

Rutgers, The State University of New Jersey, Piscataway, U.S.A.

B. Chiarito, J.P. Chou, A. Gandrakota, Y. Gershtein, E. Halkiadakis, A. Hart, M. Heindl, E. Hughes, S. Kaplan, I. Laflotte, A. Lath, R. Montalvo, K. Nash, M. Osherson, H. Saka, S. Salur, S. Schnetzer, S. Somalwar, R. Stone, S. Thomas

University of Tennessee, Knoxville, U.S.A.

H. Acharya, A.G. Delannoy, S. Spanier

Texas A&M University, College Station, U.S.A.

O. Bouhali⁷⁸, M. Dalchenko, M. De Mattia, A. Delgado, R. Eusebi, J. Gilmore, T. Huang, T. Kamon⁷⁹, H. Kim, S. Luo, S. Malhotra, D. Marley, R. Mueller, D. Overton, L. Perniè, D. Rathjens, A. Safonov

Texas Tech University, Lubbock, U.S.A.

N. Akchurin, J. Damgov, F. De Guio, V. Hegde, S. Kunori, K. Lamichhane, S.W. Lee, T. Mengke, S. Muthumuni, T. Peltola, S. Undleeb, I. Volobouev, Z. Wang, A. Whitbeck

Vanderbilt University, Nashville, U.S.A.

S. Greene, A. Gurrola, R. Janjam, W. Johns, C. Maguire, A. Melo, H. Ni, K. Padeken, F. Romeo, P. Sheldon, S. Tuo, J. Velkovska, M. Verweij

University of Virginia, Charlottesville, U.S.A.

M.W. Arenton, P. Barria, B. Cox, G. Cummings, J. Hakala, R. Hirosky, M. Joyce, A. Ledovskoy, C. Neu, B. Tannenwald, Y. Wang, E. Wolfe, F. Xia

Wayne State University, Detroit, U.S.A.

R. Harr, P.E. Karchin, N. Poudyal, J. Sturdy, P. Thapa

University of Wisconsin — Madison, Madison, WI, U.S.A.

T. Bose, J. Buchanan, C. Caillol, D. Carlsmith, S. Dasu, I. De Bruyn, L. Dodd, C. Galloni, H. He, M. Herndon, A. Hervé, U. Hussain, A. Lanaro, A. Loeliger, K. Long, R. Loveless, J. Madhusudanan Sreekala, D. Pinna, T. Ruggles, A. Savin, V. Sharma, W.H. Smith, D. Teague, S. Trembath-reichert

†: Deceased

- 1: Also at Vienna University of Technology, Vienna, Austria
- 2: Also at IRFU, CEA, Université Paris-Saclay, Gif-sur-Yvette, France
- 3: Also at Universidade Estadual de Campinas, Campinas, Brazil
- 4: Also at Federal University of Rio Grande do Sul, Porto Alegre, Brazil
- 5: Also at UFMS, Nova Andradina, Brazil
- 6: Also at Universidade Federal de Pelotas, Pelotas, Brazil
- 7: Also at Université Libre de Bruxelles, Bruxelles, Belgium
- 8: Also at University of Chinese Academy of Sciences, Beijing, China
- 9: Also at Institute for Theoretical and Experimental Physics named by A.I. Alikhanov of NRC ‘Kurchatov Institute’, Moscow, Russia
- 10: Also at Joint Institute for Nuclear Research, Dubna, Russia
- 11: Also at Cairo University, Cairo, Egypt
- 12: Now at British University in Egypt, Cairo, Egypt
- 13: Also at Purdue University, West Lafayette, U.S.A.
- 14: Also at Université de Haute Alsace, Mulhouse, France
- 15: Also at Tbilisi State University, Tbilisi, Georgia
- 16: Also at Erzincan Binali Yildirim University, Erzincan, Turkey
- 17: Also at CERN, European Organization for Nuclear Research, Geneva, Switzerland
- 18: Also at RWTH Aachen University, III. Physikalisches Institut A, Aachen, Germany
- 19: Also at University of Hamburg, Hamburg, Germany
- 20: Also at Brandenburg University of Technology, Cottbus, Germany
- 21: Also at Institute of Physics, University of Debrecen, Debrecen, Hungary
- 22: Also at Institute of Nuclear Research ATOMKI, Debrecen, Hungary
- 23: Also at MTA-ELTE Lendület CMS Particle and Nuclear Physics Group, Eötvös Loránd University, Budapest, Hungary
- 24: Also at IIT Bhubaneswar, Bhubaneswar, India

- 25: Also at Institute of Physics, Bhubaneswar, India
- 26: Also at Shoolini University, Solan, India
- 27: Also at University of Hyderabad, Hyderabad, India
- 28: Also at University of Visva-Bharati, Santiniketan, India
- 29: Also at Isfahan University of Technology, Isfahan, Iran
- 30: Now at INFN Sezione di Bari^a, Università di Bari^b, Politecnico di Bari^c, Bari, Italy
- 31: Also at Italian National Agency for New Technologies, Energy and Sustainable Economic Development, Bologna, Italy
- 32: Also at Centro Siciliano di Fisica Nucleare e di Struttura Della Materia, Catania, Italy
- 33: Also at Scuola Normale e Sezione dell'INFN, Pisa, Italy
- 34: Also at Riga Technical University, Riga, Latvia
- 35: Also at Malaysian Nuclear Agency, MOSTI, Kajang, Malaysia
- 36: Also at Consejo Nacional de Ciencia y Tecnología, Mexico City, Mexico
- 37: Also at Warsaw University of Technology, Institute of Electronic Systems, Warsaw, Poland
- 38: Also at Institute for Nuclear Research, Moscow, Russia
- 39: Now at National Research Nuclear University 'Moscow Engineering Physics Institute' (MEPhI), Moscow, Russia
- 40: Also at St. Petersburg State Polytechnical University, St. Petersburg, Russia
- 41: Also at University of Florida, Gainesville, U.S.A.
- 42: Also at Imperial College, London, United Kingdom
- 43: Also at P.N. Lebedev Physical Institute, Moscow, Russia
- 44: Also at California Institute of Technology, Pasadena, U.S.A.
- 45: Also at INFN Sezione di Padova^a, Università di Padova^b, Padova, Italy, Università di Trento^c, Trento, Italy
- 46: Also at Budker Institute of Nuclear Physics, Novosibirsk, Russia
- 47: Also at Faculty of Physics, University of Belgrade, Belgrade, Serbia
- 48: Also at Università degli Studi di Siena, Siena, Italy
- 49: Also at INFN Sezione di Pavia^a, Università di Pavia^b, Pavia, Italy
- 50: Also at National and Kapodistrian University of Athens, Athens, Greece
- 51: Also at Universität Zürich, Zurich, Switzerland
- 52: Also at Stefan Meyer Institute for Subatomic Physics, Vienna, Austria
- 53: Also at Burdur Mehmet Akif Ersoy University, BURDUR, Turkey
- 54: Also at Şırnak University, Sirnak, Turkey
- 55: Also at Tsinghua University, Beijing, China
- 56: Also at Beykent University, Istanbul, Turkey
- 57: Also at Istanbul Aydin University, Application and Research Center for Advanced Studies (App. & Res. Cent. for Advanced Studies), Istanbul, Turkey
- 58: Also at Mersin University, Mersin, Turkey
- 59: Also at Piri Reis University, Istanbul, Turkey
- 60: Also at Gaziosmanpasa University, Tokat, Turkey
- 61: Also at Ozyegin University, Istanbul, Turkey
- 62: Also at Izmir Institute of Technology, Izmir, Turkey
- 63: Also at Marmara University, Istanbul, Turkey
- 64: Also at Kafkas University, Kars, Turkey
- 65: Also at Istanbul Bilgi University, Istanbul, Turkey
- 66: Also at Hacettepe University, Ankara, Turkey
- 67: Also at Adiyaman University, Adiyaman, Turkey
- 68: Also at Vrije Universiteit Brussel, Brussel, Belgium

- 69: Also at School of Physics and Astronomy, University of Southampton, Southampton, United Kingdom
- 70: Also at IPPP Durham University, Durham, United Kingdom
- 71: Also at Monash University, Faculty of Science, Clayton, Australia
- 72: Also at Bethel University, St. Paul, Minneapolis, U.S.A.
- 73: Also at Karamanoğlu Mehmetbey University, Karaman, Turkey
- 74: Also at Bingol University, Bingol, Turkey
- 75: Also at Georgian Technical University, Tbilisi, Georgia
- 76: Also at Sinop University, Sinop, Turkey
- 77: Also at Mimar Sinan University, Istanbul, Turkey
- 78: Also at Texas A&M University at Qatar, Doha, Qatar
- 79: Also at Kyungpook National University, Daegu, Korea

2020 JINST 15 P02027